Journal Pre-proof

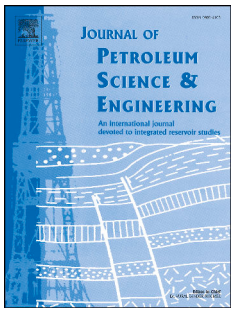

Experimental study on hydrate saturation evaluation based on complex electrical conductivity of porous media

Lanchang Xing, Jiale Niu, Shuli Zhang, Shengchang Cao, Bin Wang, Liyun Lao, Wei Wei, Weifeng Han, Xinmin Ge, Zhoutuo Wei

PII: S0920-4105(21)01178-5

DOI: https://doi.org/10.1016/j.petrol.2021.109539

Reference: PETROL 109539

To appear in: *Journal of Petroleum Science and Engineering*

Received Date: 2 May 2021

Revised Date: 17 September 2021

Accepted Date: 18 September 2021

Please cite this article as: Xing, L., Niu, J., Zhang, S., Cao, S., Wang, B., Lao, L., Wei, W., Han, W., Ge, X., Wei, Z., Experimental study on hydrate saturation evaluation based on complex electrical conductivity of porous media, *Journal of Petroleum Science and Engineering* (2021), doi: https://doi.org/10.1016/j.petrol.2021.109539.

Credit author statement

Lanchang Xing: Conceptualization, Methodology, Investigation, Formal analysis, Writing – original draft, Writing - review & editing, Project administration;

Jiale Niu, Shuli Zhang, Shengchang Cao, Bin Wang: Validation, Data curation and analysis, Visualization, Writing - review & editing;

Liyun Lao, Wei Wei, Weifeng Han: Resources, Data analysis, Writing - review & editing

Xinmin Ge, Zhoutuo Wei: Data analysis, Writing - review & editing

Journal of Petroleum Science and Engineering, Volume 208, Part C, January 2022, Article number 109539
DOI:10.1016/j.petrol.2021.109539

Experimental study on hydrate saturation evaluation based on complex electrical conductivity of porous media

Lanchang Xing[1,*], Jiale Niu[1], Shuli Zhang[1], Shengchang Cao[1], Bin Wang[1],

Liyun Lao[2], Wei Wei[3], Weifeng Han[3], Xinmin Ge[4], Zhoutuo Wei[4]

[1] College of Control Science and Engineering, China University of Petroleum (East China), No. 66, West Changjiang Road, Huangdao District, Qingdao 266580, China

[2] School of Water, Energy and Environment, Cranfield University, Cranfield MK43 0AL, UK

[3] Department of Alternative Energy, PetroChina Research Institute of Petroleum Exploration & Development, Langfang 065007, Hebei, China

[4] School of Geosciences, China University of Petroleum (East China), Qingdao 266580, Shandong, China

[*] Correspondence: xinglc@upc.edu.cn OR l.xing@yahoo.com

Abstract

The hydrate saturation is a critical parameter in the evaluation of gas hydrate reservoirs. The complex characteristics of hydrate-bearing sediments pose challenges to the reliability of conventional geophysical techniques for hydrate saturation evaluation. In this paper, we present a study on developing a novel approach to characterize the electrical properties of hydrate-bearing porous media and to evaluate the hydrate saturation quantitatively based on parameters of the complex electrical conductivity. In the laboratory experiments we prepared samples with the tetrahydrofuran hydrate forming in sands to simulate the hydrate-bearing sediments and for measuring the complex conductivity at frequencies from 20 Hz to 100 kHz. The frequency-dispersion

characteristics of complex conductivity of the hydrate-bearing samples with different saturations were analyzed, and then three types of hydrate-saturation evaluation models, denoted as the conductance-based, polarization-based and fusion models, were developed based on the in-phase conductivity, frequency-dispersion characteristic parameters of the phase angle and the combination of those two, respectively. A critical frequency (f_c = 2 kHz) can be identified, where both the phase angle and imaginary component of the complex conductivity reach their minima. The Archie's formula shows its capability to model the relationship between the in-phase conductivity and hydrate saturation (i.e., conductance-based model), but the frequency higher than f_c is preferred because stable Archie parameters can only be obtained in that frequency range. Linear correlations between the hydrate saturation and frequency-dispersion characteristic parameters (i.e., the logarithms of FE (frequency effect) and slope of the relation between FE and FR (frequency ratio) of the phase angle can be obtained, serving as the polarization-based models in the frequency range higher than f_c. The fusion model performs the best in the perspective of low errors and high reliability for predicting the hydrate saturation, because more parameters of the complex conductivity and underlying physics of the conductance and polarization have been incorporated. In the frequency range lower than f_c in contrast to that of the phase angle, the quadrature conductivity shows remarkable frequency-dispersion characteristics with the variation of the hydrate saturation, showing the great potential for developing new saturation-evaluation models in future.

Keywords: hydrate saturation, complex electrical conductivity, frequency dispersion, conductance, polarization, information fusion

1 Introduction

Natural gas hydrates exist widely in marine sediments and land permafrost over the world. It has been considered as a new type of unconventional energy source, which has a great potential for the natural gas supply (Collet, 2002; Milkov, 2004; Moridis et al., 2009, 2011; Makogon, 2010; Koh et al., 2012). Compared with the conventional oil and gas, the reservoirs of natural gas hydrate exhibit unique and complex characteristics as follows: the hydrate exists in a solid state and exhibits various micro-distribution modes in formations; the fracture type, fine-grained, unconsolidated sediments with clays are common in reservoirs; the hydrate tends to decompose and reform due to its sensitivity to temperature and pressure variations. The solid-state hydrates with various micro/macro-scale occurrence morphologies in the formations result in the heterogeneity of the pore-water distribution and anisotropy of the reservoir physical properties (Kennedy and Herrick, 2004; Lee and Collet, 2009; Cook et al., 2012; Yin et al., 2019b; Wu et al., 2020, 2021a). Additionally, the instability of hydrates and subsequent decomposition/reformation can cause unpredictable variations in the pore-water salinity (Ning et al., 2013ab; Santamarina et al., 2015; Yang et al., 2019). To sum up, the particularity and complexity pose severe challenges to a quantitative evaluation of hydrate reservoirs. The degree of hydrate saturation (i.e., the volume ratio of hydrate to pore space of the formation) is a key parameter in the evaluation of gas hydrate reservoirs, because it directly affects the accuracy and reliability for estimating the gas resource therein and designing the production strategies. Geophysical logging techniques play an irreplaceable role in the identification of hydrate reservoirs and the evaluation of geophysical properties of the formations. As the electrical resistivity and elastic-wave velocity are most affected by hydrates in the formations (higher resistivity and velocity than gas/water-bearing formations), the resistivity and acoustic logging have become effective techniques to evaluate the hydrate saturation (Lee et al., 1996; Riedel et al., 2005; Shankar and Riedel, 2011; Cook and Waite, 2018). Since hydrates usually occur in sediments with a poor consolidation degree, and the

acoustic wave is more easily affected by the compaction coefficient (Priest et al., 2005; Winters et al., 2007; Priest et al., 2009), the resistivity logging is relatively more stable and reliable (Lee and Collet, 2008). However, the conventional resistivity logging technique is affected by various factors, such as the formation lithology and pore-water salinity (Ning et al., 2013ab), significantly. Furthermore, the complex and particular characteristics of hydrate reservoirs stated above seriously restrict the accuracy and reliability of hydrate-saturation evaluation by the resistivity logging technique.

The complex electrical resistivity/conductivity approach has been used to characterize the properties of porous materials such as soils, sandy and clayed sandstones (Revil et al., 2013, 2017ab). Based on the parameters derived from complex-conductivity spectra, some reservoir or petrophysical parameters, such as the pore structure, specific surface area, wettability, permeability, porosity and saturation of fluids in porous media have been evaluated successfully. Ruffet (1991) measured the complex resistivity on saturated samples and found that the frequency dependence of the complex resistivity in the frequency range of 1 kHz – 1 MHz presented a clear correlation with the surface area. Denicol and Jing (1996) calculated the slope of the electrical impedance versus the logarithm of frequency within a range of 10 – 100 kHz, and then correlated it with the permeability and the clay volume (Denicol and Jing, 1998). Moss et al. (2002) illustrated that the wettability affected the correlation between the degree of frequency dispersion and the saturation, and subsequently claimed that the reservoir wettability could be evaluated by the resistivity measurements at frequencies from 10 kHz to 1 MHz. Tong and Tao (2008) combined the porosity and the frequency dependency of the imaginary resistivity within the range of 100 Hz – 1.5 kHz to estimate the permeability of shaly sandstones. Zisser and Nover (2009) analyzed measurements of the complex resistivity on tight sandstones within the range of 10 kHz – 1 MHz using the Cole-Cole model (Cole and Cole, 1941) and the model developed by Lysne (1983), however, they concluded

that it was impossible to estimate the permeability from the relaxation time or formation factor. Weller et al. (2010) measured the complex resistivity of sandstones in the frequency range of 2.8 mHz – 750 kHz and then developed a power-law correlation to predict the permeability by using the resistivity, chargeability and mean relaxation time derived from the Debye decomposition (Nordsiek and Weller, 2008). Revil et al. (2015) tested their permeability prediction model (Revil et al., 2012), which accepted the characteristic relaxation time, intrinsic formation factor and a diffusion coefficient as inputs, using a broad collection of complex conductivity data on pure silica, clean sands or sandstones and clayey materials. Following the modeling approach proposed for shaly sandstones by Tong and Tao (2008), Norbisrath et al. (2017) analyzed the complex-resistivity spectra measured on core plugs from a wide variety of carbonates in the range of 10 – 100 kHz, and predicted the pore-geometry related petrophysical parameters such as permeability and cementation factor. Jiang et al. (2018) conducted numerical and experimental studies on the development of a complex-resistivity-logging tool for evaluating low-resistivity reservoirs. The water saturation was estimated from the relaxation time constant, which was derived from a best fitting of the complex resistivity spectra (1 – 500 kHz) with the Cole-Cole model. To investigate the application of the complex-resistivity logging method in sand-shale reservoirs, Li et al. (2019) performed measurements of the complex resistivity on both clear and shaly sand samples in the range of 40 Hz – 1 MHz. They established a relationship between the water saturation, porosity and time constant (derived from a best fitting with the Cole-Cole model) based on the Archie model (Archie, 1942) and Waxman-Smith model (Waxman and Smith, 1968). The complex-resistivity logging approach was proposed based on the application of the induced polarization method to boreholes (Freedman, 1986; Worthington and Collar, 1984; Osterman et al., 2016). It has been used to identify and evaluate oil, gas and water formations due to their differences in the induced-polarization responses. The complex resistivity is mainly affected by the oil saturation, while the lithology and pore-water salinity become secondary factors (Jiang et al., 2018; Li et al., 2019). Therefore, the

complex-resistivity logging approach has remarkable advantages in determining the oil saturation of reservoirs and flooding degree of water-flooded reservoirs. Considering the similarity of the electrical properties between oil and hydrate, and the varying pore-water salinity in the hydrate decomposition/reformation processes, the complex resistivity logging method may become a preferable solution to the problem of hydrate saturation evaluation.

In this paper, a new approach for characterizing the electrical properties of hydrate-bearing porous media as well as evaluating the hydrate saturation was developed based on laboratory measurements and modelling analysis of complex conductivity parameters. In the laboratory experiments we prepared tetrahydrofuran (THF) hydrate-bearing sandy samples and then measured the complex conductivity at frequencies from 20 Hz to 100 kHz. Subsequently, the frequency-dispersion characteristics of complex conductivity were analyzed, and then three types of hydrate-saturation evaluation models with complex-conductivity parameters as inputs were developed based on the electrical conductance mechanism, low-frequency electrical polarization mechanism and information fusion principle, respectively. The models were then assessed and compared based on an analysis of prediction errors to demonstrate their strengths and drawbacks. A discussion section was then presented on the potential for building hydrate-saturation evaluation models with the quadrature conductivity, advances and issues related to the THF hydrate-bearing samples and issues for extending the approach proposed in this work to gas hydrate-bearing sediments. At the end, this work is concluded and some future work is proposed. The complex-conductivity based approach proposed in this work provides a novel and powerful tool to evaluate the hydrate saturation in porous media as well as to obtain more understanding on the electrical properties of hydrate-bearing sediments. The experimental data and hydrate-saturation evaluation models provide a foundation for developing new complex-conductivity based geophysical exploration techniques for

evaluating natural gas hydrate reservoirs.

2 Methods

2.1 Complex conductivity of porous media

The effective electrical properties of porous media (e.g., the unconsolidated sediments, consolidated rocks in formations), which describe the electrical conduction and polarization effects, can generally be represented by the complex-valued electrical conductivity (complex conductivity σ^* hereafter). This complex quantity can be expressed in terms of the magnitude and phase angle or real and imaginary components (as shown in Eq. (1)). The real and imaginary components of complex conductivity are called the in-phase and quadrature conductivities, respectively (Tarasov and Titov, 2013).

$$\sigma^*(\omega) = |\sigma(\omega)| e^{i\varphi(\omega)} = \sigma'(\omega) + i\sigma''(\omega) \tag{1}$$

where i is the imaginary unit, ω (in rad) denotes the angular frequency ($\omega = 2\pi f$, with the unit of the frequency f as Hz); σ' (in S/m) is the in-phase conductivity, i.e., the real component of σ^*, σ'' (in S/m) is the quadrature conductivity, i.e., the imaginary component of σ^*, $|\sigma|$ is the magnitude of σ^*, and φ (in rad) is the phase angle of σ^*. The relationship between σ', σ'' and φ is given by Eq (2).

$$\varphi(\omega) = \arctan\left[\frac{\sigma''(\omega)}{\sigma'(\omega)}\right] \tag{2}$$

Generally, the complex conductivity of a porous medium with a water solution in the pores is frequency dependent. The in-phase conductivity relates to the current flow via electromigration mechanism, while the quadrature conductivity represents the polarization process (Vinegar and Waxman, 1984). The low-frequency polarization (e.g., lower than 1 MHz) can be attributed to the chemical capacitance and the true dielectric effects (Revil, 2013).

The in-phase conductivity can be described by the model of Jougnot et al. (2010) based on Revil et al. (2007)

for variably water-saturated porous media as Eq. (3).

$$\sigma' = \frac{1}{F}\sigma_w S_w^n + \left(\frac{F-1}{F}\right)\sigma_s' \tag{3}$$

where F (dimensionless) is the formation factor, σ_w (in S/m) is the conductivity of the pore water, S_w (dimensionless) is the water saturation, n is the saturation exponent and σ_s' is the real component of the surface conductivity. The detailed expression for calculating σ_s' can be found in Leroy et al. (2008). It has been demonstrated that this model fits the real component of the complex conductivity data well (Breede et al., 2012).

2.2 Saturation calculation with Archie's formula

The formation factor of a sandstone can be related to its porosity based on the first Archie's law (Archie, 1942). For a sandstone fully saturated with a brine, the relationship between the bulk conductivity and porosity can be expressed as Eq (4).

$$F = \frac{\sigma_w}{\sigma_0} = a\phi^{-m} \tag{4}$$

where ϕ (dimensionless) is the porosity of the sandstone, m (dimensionless) is the cementation exponent, σ_0 (in S/m) is the bulk conductivity of the sandstone saturated with the brine, σ_w (in S/m) is the conductivity of the brine and a (dimensionless) is a coefficient. When the sandstone is saturated with brine and oil, the relationship between the conductivity and the water saturation (S_w) can be obtained based on the second Archie's law.

$$I = \frac{\sigma_0}{\sigma_t} = bS_w^{-n} \tag{5}$$

where I (dimensionless) is the conductivity index, σ_t (in S/m) is the conductivity of the sandstone saturated with the brine and oil, n (dimensionless) is the saturation exponent and b (dimensionless) is a coefficient. The parameters a, b, m and n need to be determined based on experimental data and/or through a numerical approach.

In the case of the complex conductivity, the conductivity term in Eqs. (4) and (5) may be replaced with the in-phase or quadrature conductivity at a specific frequency (Li et al., 2019; Xing et al., 2020; Xing et al., 2021). However, the parameters *a*, *b*, *m* and *n* have to be determined and interpreted carefully to obtain a reliable prediction of the water saturation.

2.3 Frequency dispersion of complex conductivity

The frequency dependence of complex conductivity is also referred to as the frequency dispersion. To evaluate the characteristics of frequency dispersion quantitatively, a parameter FE (frequency effect) was originally defined as the fractional ratio of the resistivity change between any two frequencies as expressed by Eq. (6) by Vinegar and Waxman (1984).

$$\mathrm{FE} = \frac{\rho(\omega) - \rho(A\omega)}{\rho(\omega)} \tag{6}$$

where ρ is the resistivity, A is a multiple of the frequency (ω) of interest.

The parameter FE was defined based on the resistivity in its original form, but it can be modified by substituting it with the magnitude, phase angle, real component or imaginary component of complex conductivity to demonstrate the frequency dispersion characteristics of those electrical parameters (Revil et al., 2017b).

3 Experimentation

3.1 Experimental setup

The experimental setup is composed of two parts, i.e., the environment simulation part and measurement part. The environment simulation part includes a reactor and an air bath incubator providing a space and low-

temperature environmental conditions for the growth of hydrates. The measurement part includes sensors, an impedance measurement instrument, data acquisition cards and a control computer with a set of self-developed software for the instrument control, data acquisition, signal preprocessing, information displaying and data storage. The schematic diagram of the experimental setup is shown in **Fig. 1**.

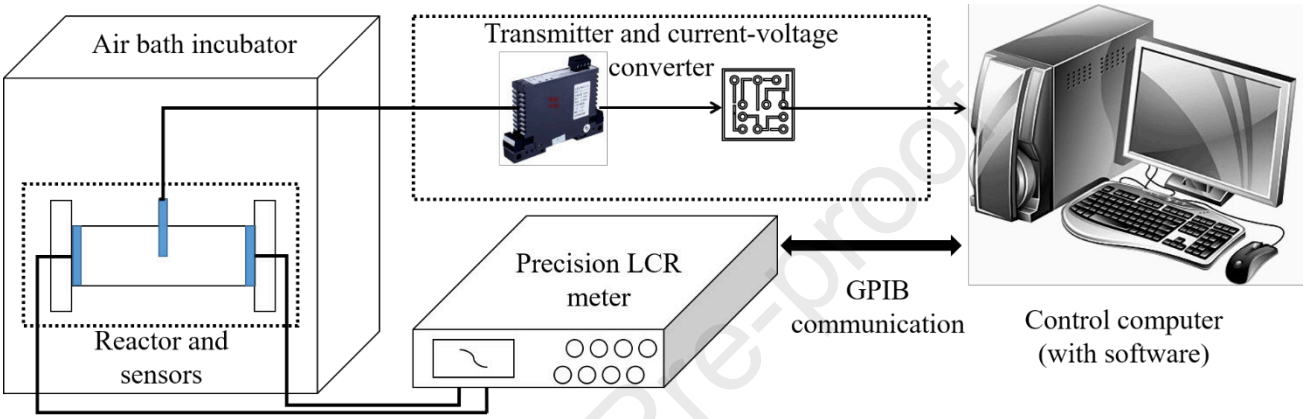

LCR: Inductance, Capacitance and Resistance; GPIB: General-Purpose Interface Bus

Fig. 1 Schematic diagram of the experimental setup

The reactor was designed as a cylinder with the inner diameter of 40 mm and the length of 100 mm as shown in **Fig. 2**. The acrylic material was used due to its good performance in the heat transfer, electrical insulation, corrosion resistance and visual observation. Two blind flanges were installed at the two ends to keep a cylindrical shape of the tested sample. Two disk-shaped electrodes were fixed firmly on the inner sides of the blind flanges, respectively, through the epoxide resin. The electrodes were made from copper with the thickness of 0.1 mm and the diameter of 40 mm. A resistance temperature detector (RTD) was inserted into the reactor through a drilled hole with the diameter of 3 mm. The reactor was placed in the air bath incubator, in which the ambient temperature was controlled automatically with a variation less than 0.25 °C.

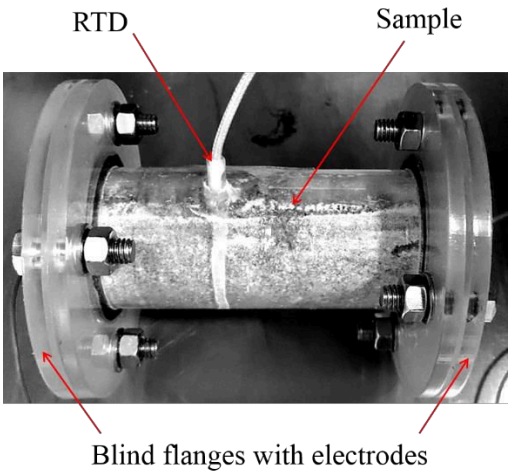

Fig. 2 Picture of the reactor and sensors (RTD denotes the Resistance Temperature Detector)

The electrical impedance (denoted as Z^*) of the sample between the two electrodes was measured with an Agilent precision LCR (inductance, capacitance, and resistance) meter (Model 4284A). The LCR meter measures 22 sets of electrical impedance with the uncertainty of 0.1% in the frequency range of 20 Hz to 1 MHz for each sample. It was controlled by the control computer through a self-developed software with Matlab® and GPIB (General-Purpose Interface Bus) protocol. The temperature in the reactor was measured by the RTD (Pt100 with the uncertainty of 0.15°C) and the resistance change was converted into a voltage signal through a transmitter and current-voltage converter before sampled by the data acquisition card (model number PCI-1747U). The card was controlled by the control computer through a self-developed software with LabVIEW®. By utilizing the above two sets of self-developed software (Xing et al., 2020), parameters of the LCR meter and data acquisition card were configured flexibly and then the measured data were transmitted to the control computer in a real-time mode.

The complex conductivity σ^* can be related to Z^* via the complex resistivity ρ^* and a geometrical factor K_g (in meters) as below (Zhang et al, 2017):

$$\sigma^* = \frac{1}{\rho^*} = \frac{1}{K_g Z^*} \tag{7}$$

The geometrical factor takes into account the geometry and positions of the electrodes relative to the sample under test. The geometrical factor is calculated as 0.004π m in the experiment of this work.

3.2 Sample preparation and parameter test

Tetrahydrofuran (THF) was selected as the hydrate former (Pearson et al., 1986; Santamarina and Ruppel, 2008; Cortes et al., 2009; Yun et al., 2007; Lee et al., 2007; 2010ab; Liu et al., 2019; Wu et al., 2021a). NaCl aqueous solution prepared with deionized water was used as the pore water. Natural sea sand filtered with griddles was used to simulate the unconsolidated porous medium. The size of the sand particles used in this study ranges from 180 to 250 μm in diameter. The particles of this size range fall into the category of fine sands (63 to 250 μm) according to the criteria proposed by Shepard (1954). The particle size distribution of natural sediments containing gas hydrates typically spans a broad range. For the Shenhu area (South China Sea) it is reported by (Zhang, et al., 2007) that the gas hydrates occur homogeneously in extremely fine-grain sediments. This is unique among known marine gas hydrate deposits such as the coarse grains from Nankai Trough offshore Japan (Uchida and Takashi, 2004) and southern Hydrate Ridge offshore Oregon (Tréhuet al., 2004, 2003, 2006). An analysis of the samples of hydrate-bearing sediments recovered from SH2 and SH7 has shown that the silty fine sand and silty medium-fine sand dominate the sediments, respectively (Shepard, 1954; Liu et al., 2012; Liu et al., 2017; Wang et al., 2011). In this work, a narrow range of particle size distribution (180 to 250 μm) within the category of fine sands was adopted in order to not only represent the fine-grained sediments to some extent, but also alleviate the difficulty in forming hydrates in extremely fine sediments (e.g., silt, clay etc., Wu et al., 2021b) and reduce the possibility of heterogeneity in the host skeleton. We regarded the sand particles were of the same level of sizes due to the narrow range, thus the size distribution was assumed to follow a normal distribution.

Furthermore, the high specific surface area and strong cation exchange capacity of clays influence the low-frequency complex-conductivity responses significantly (Revil et al., 2013). The effect of clays on the complex-conductivity responses of hydrate-bearing sediments deserves a dedicated future work.

The hydrate saturation (denoted as S_h ranging from 0 to 1) in the sample can be calculated from the quantity of consumed THF, with the assumption that all the THF added into the sample has been transformed into hydrate (The issues related to this assumption will be discussed in Section 5.3.). The chemical formula of THF hydrate is $C_4H_8O \cdot 17H_2O$, indicating that 1 mol THF and 17 mol H_2O are required to synthesize 1 mol THF hydrate. The saturation of THF hydrate in the sample is defined as the volume ratio of hydrate to that of the pore space in the porous medium. In the experiment of this work, the THF hydrate saturation in the sandy sample was determined by calculating the water saturation as expressed by Eq. (8). Then the hydrate saturation is obtained by $S_h = 1 - S_w$.

$$S_w = \frac{\left(\frac{m_w}{M_w} - \frac{17 m_{\mathrm{THF}}}{M_{\mathrm{THF}}} \right) M_w}{\rho_w V_{\mathrm{sand}} \phi} \tag{8}$$

where m_w (in g) and m_{THF} (in g) are the masses of the pore water and THF in the sample under test at the initial state (i.e. no hydrate), respectively; M_w and M_{THF} are the molar masses of the pore water and THF, respectively (M_w = 18 g/mol, M_{THF} = 72 g/mol); ρ_w (in g/mL) is the density of the pore water; V_{sand} (in mL) is the bulk volume of the sandy sample (i.e., the total volume of sand particles and pores); ϕ is the porosity of the sandy sample (ϕ = 0.4 for the tested sandy sample in this work).

The hydrate-bearing sandy samples were prepared and tested following the procedures stated below:

(1) Preparation of the sand and THF solution. The filtered sand was rinsed, screened and dried, and then an appropriate amount (slightly more than the volume of the reactor) of sand was taken out for use. The pore water (i.e., NaCl solution) was prepared by mixing the denoised water with a proportional amount of NaCl. The initial mass fraction of NaCl in the pore water is 0.24%, 0.46%, 0.66% and 0.84% for the hydrate saturation of 0.8, 0.6, 0.4 and 0.2, respectively. Different initial concentrations were used to ensure that the mass fraction of NaCl in the final state of the pore water, i.e., in the remaining pore water at the end of the hydrate formation process, is 1.0%. Then the THF solution was obtained by adding an appropriate amount of THF (according to Eq. (8)) to the pore water prepared above.

(2) Loading of the sand and THF solution into the reactor. The sand was loaded into the reactor layer by layer and the THF solution was injected into the newly added layer to ensure that the sand pack in the reactor was fully saturated with the solution. The sand pack in the reactor was compacted with a rubber rod after each addition of the sand layer and solution. Finally, the sand pack was squeezed through the two blind flanges with electrodes on the two ends of the reactor. An extra amount of the solution could be squeezed out from the sand pack, indicating the sand pack was fully saturated with the THF solution. The net mass of the injected solution and volume of the sand pack were measured, and then the porosity of the sand pack was determined.

(3) Formation of the THF hydrate in the reactor. The reactor filled with a mixture of the sand and THF solution was placed into the air bath incubator (as shown in **Fig. 1**). A temperature much lower than 4.4 °C (i.e., the equilibrium temperature) for synthesizing the THF hydrate was set to the air bath incubator (e.g., −1.0 °C). Then the cooling mode of the air bath incubator was triggered and the formation process of the THF hydrate was initiated. The hydrate formation process lasted for about 24 hours.

(4) Measurement of the electrical impedance of the sample. After the hydrate formation process finished, the electrical impedance of the hydrate-bearing sample was measured at ten frequencies (20 Hz, 100 Hz, 200 Hz, 500 Hz, 1 kHz, 2 kHz, 5 kHz, 10 kHz, 50 kHz and 100 kHz) and the test was repeated for ten times. The measurement was repeated every 30 minutes until no significant variations between the repeated measurements could be found. Finally, the test process was terminated by stopping the cooling mode of the air bath incubator, then the hydrate dissociation process was triggered under the condition of room temperature (e.g., 25 °C).

3.3 Processes of hydrate formation and decomposition

The variations of the complex conductivity with time at different frequencies (20 Hz, 100 Hz, and 10 kHz) are shown in **Fig. 3**. The time trace of the temperature is also plotted to illustrate the evolution of the experiment, which includes the processes of hydrate formation and decomposition. It can be seen that the quadrature conductivity of the complex conductivity is much smaller than the in-phase conductivity. As a result, the magnitude of the complex conductivity is quite close to the in-phase conductivity (not presented for brevity). The experimental process of each test run can be divided into four stages (as shown in **Fig. 3**) according to the variations of the temperature and complex conductivity. It needs to be mentioned that the division of the hydrate formation and decomposition processes is not deterministic, but only used to help understand the characteristics of the complex-conductivity responses and the evolution of the experimental process.

- **Stage 1**. The first stage defines itself in the time period when the temperature decreases from the ambient temperature (e.g., around 12 °C in the experiment) to the starting point of the hydrate formation. The in-phase conductivity decreases with the reduced mobility of ions due to the decrease of the temperature.

- **Stage 2.** In the second stage the THF hydrate forms at varying formation rates. A higher formation rate is indicated by the sudden rise of the temperature. Complex variations of the in-phase conductivity with time emerge over this stage due to the phase change from the THF solution to a mixture of the solution and THF hydrate. The starting point of this stage is located at around 2.83 h, where the temperature is around 0.7 °C.
- **Stage 3.** After all the hydrate former (i.e., THF) is consumed the process returns into peace indicated by the steady time traces of the temperature and in-phase conductivity in the third stage. The void space of the porous medium (i.e., the sand pack) is filled with the THF hydrate and remaining NaCl solution.
- **Stage 4.** In the last stage the temperature increases gradually, but there is a section (starting around 4.4 °C) characterized by a lower increasing rate with time indicating that the hydrate decomposes then.

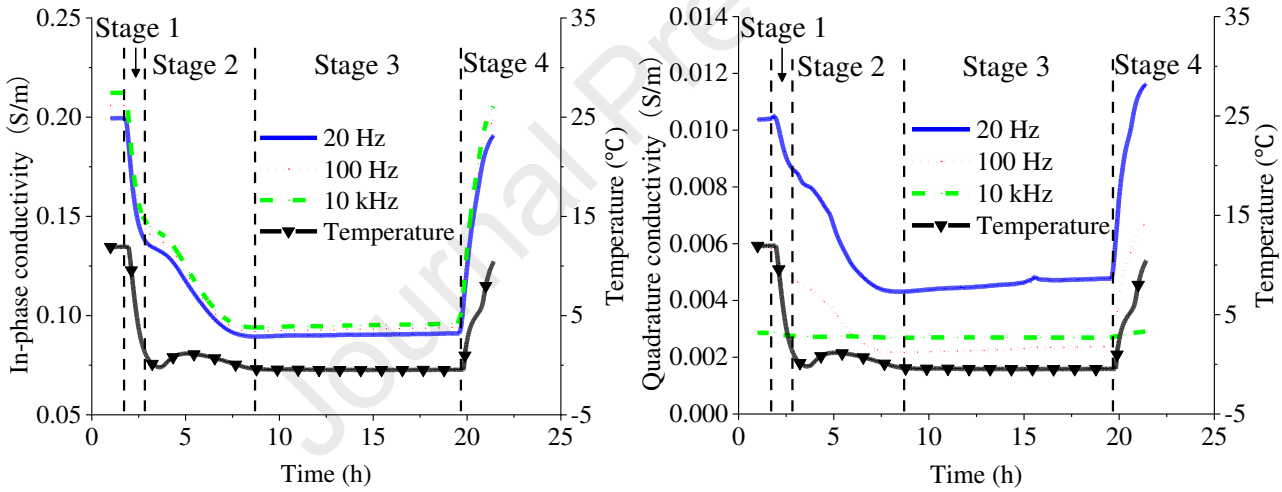

(a) In-phase conductivity and temperature (b) Quadrature conductivity and temperature

Fig. 3 Time traces of the complex conductivity and temperature in the processes of hydrate formation and decomposition

4 Results and analysis

4.1 Effects of frequency and saturation on complex conductivity

To illustrate the frequency effect on the complex conductivity in the hydrate formation process introduced in

Section 3.3, a typical time point corresponding to a certain hydrate saturation is selected in each stage as shown in **Fig. 3**. The values of the selected hydrate saturations follow a relationship of $S_{h1} < S_{h2} < S_{h3}$. The magnitude, phase angle, real and imaginary components of the complex conductivity corresponding to the three saturations are plotted versus frequency in **Fig. 4**.

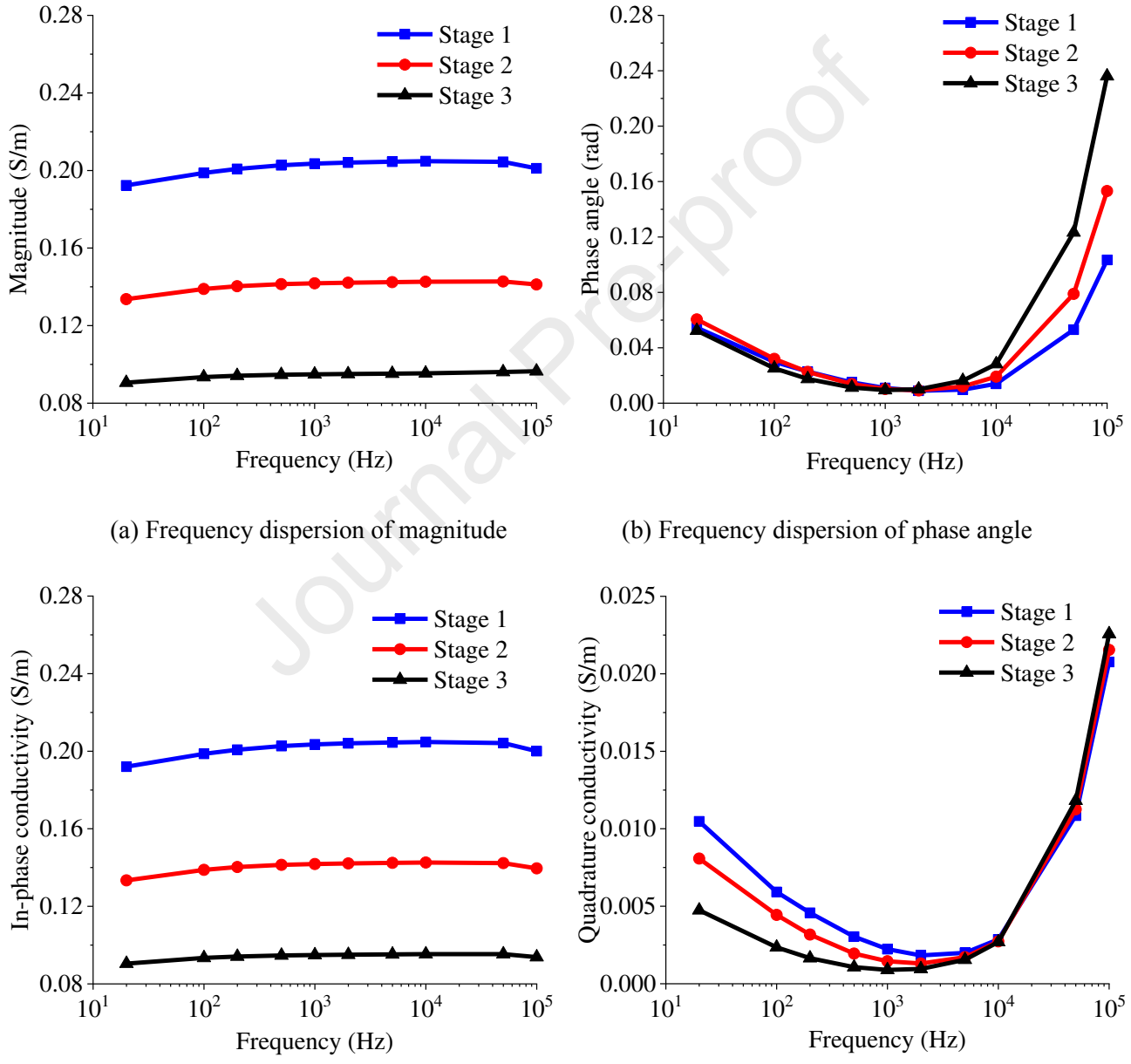

(a) Frequency dispersion of magnitude (b) Frequency dispersion of phase angle

(c) Frequency dispersion of in-phase conductivity (d) Frequency dispersion of quadrature conductivity

Fig. 4 Frequency dispersion of parameters of the complex conductivity

The phase angle and quadrature conductivity exhibit significant variations with frequency and a minimum can be found at a certain frequency. This frequency is called 'critical frequency' (denoted as f_c) hereafter according to the references, e.g., Tong and Tao (2008) and Li et al. (2019). A consistent critical frequency around 2 kHz can be identified for the phase angle and quadrature conductivity, thus f_c = 2 kHz is adopted throughout this work. It is postulated that different polarization mechanisms dominate in the frequency ranges lower and higher than this critical frequency (Revil, 2013; Chelidze and Gueguen, 1999; Chelidze et al., 1999). The electrical double layer (EDL) polarization dominates the electrical polarization process in the lower frequency range ($f < f_c$), where the phase angle and quadrature conductivity decrease with the increase of the frequency as shown in **Fig. 4b and 4c**. When the frequency is greater than the critical frequency ($f > f_c$), the interfacial polarization (i.e., Maxwell-Wagner effect) tends to dominate the polarization process. The in-phase conductivity and phase angle increase with an increasing frequency, which can be evidenced by the interfacial polarization mechanism (Chen and Or, 2006ab). Compared with the phase angle of the complex conductivity and quadrature conductivity, the in-phase conductivity exhibits minor frequency-dispersion characteristics. This is reasonable because the frequency has minor effects on the electrical conduction process.

It can be observed in **Fig. 4** that the magnitude of complex conductivity and in-phase conductivity decreases significantly with the increase of the hydrate saturation, while the phase angle and quadrature conductivity present inconsistent behavior in different frequency ranges separated by the critical frequency. The difference in the frequency dispersion of the phase angle for different hydrate saturations can only be found in the frequency range $f > f_c$ (as shown in **Fig. 4b**), while that of the quadrature conductivity can only be identified in the frequency range $f < f_c$ (as shown in **Fig. 4d**). To evaluate the frequency-dispersion characteristics

quantitatively, a parameter FE was proposed in Vinegar and Waxman (1984) as shown in Eq. (6). The parameter FE is modified by substituting the resistivity with parameters of complex conductivity, i.e., the phase angle and quadrature conductivity, in this work, as shown in Eqs. (9) and (10).

$$\mathrm{FE} = \left| \frac{\varphi(f_H) - \varphi(f_L)}{\varphi(f_L)} \right| \tag{9}$$

and

$$\mathrm{FE} = \left| \frac{\sigma''(f_H) - \sigma''(f_L)}{\sigma''(f_L)} \right| \tag{10}$$

where f_H and f_L denote higher and lower frequencies of interest, respectively.

The variations of FE for the three saturations above are plotted against frequency in **Fig. 5** (with f_L = 20 Hz and f_L = 2 kHz for the phase angle and quadrature conductivity, respectively). It can be seen that the parameter FE increases with an increasing f_H. This is reasonable because a larger difference in the phase angle and quadrature conductivity can be obtained with a larger frequency difference between f_H and a fixed f_L. Furthermore, with the increase of S_h, the FE at the same f_H and thus the same frequency ratio (FR = f_H / f_L) for both the phase angle and quadrature conductivity increases (i.e., a higher FE corresponding to a higher S_h). It is clearly shown in **Fig. 5** that the difference in S_h can be discriminated by the parameter FE, which implies a dependence of the FE on S_h for a fixed FR.

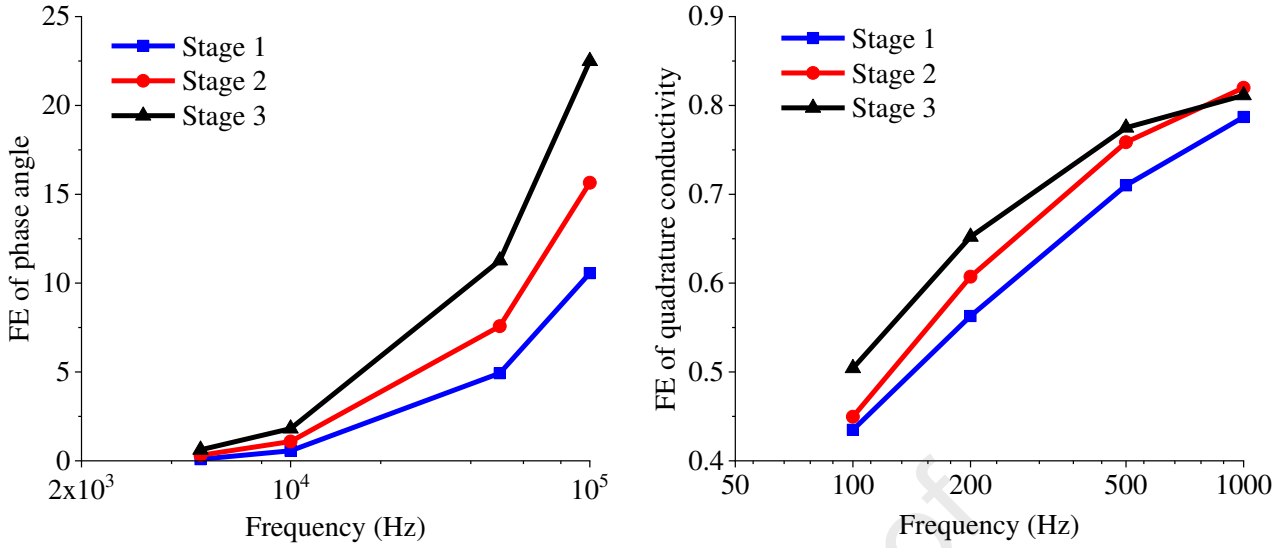

(a) FE of phase angle against f_H

(b) FE of quadrature against f_H

Fig. 5 Variations of the parameter FE with the higher frequency f_H at a fixed f_L

4.2 Saturation model based on electrical conductance mechanism

The complex conductivity responses of hydrate-bearing sample at different saturations, i.e., S_h = 0.2, 0.4, 0.6 and 0.8, were measured in the experiment. As described in **Section 3**, the hydrate saturation was obtained by calculating the quantity of consumed THF, assuming that all the THF in the solution was transformed into THF hydrate. The in-phase conductivity describes the conduction process (based on the Ohmic electromigration mechanism) of the electrical current in the hydrate-bearing sample, thus the classical model, i.e., Archie formula, has been used for evaluating the hydrate saturation based on the in-phase conductivity in this section.

The in-phase conductivity is plotted versus frequency in **Fig. 6** for different hydrate saturations, i.e., S_h = 0.2, 0.4, 0.6 and 0.8. It can be observed that the in-phase conductivity varies little with the frequency. This is expected because the in-phase conductivity is controlled by the electrical conductance mechanism of the sample under test. Under the condition of a fixed frequency of interest, the in-phase conductivity exhibits a monotonously decreasing trend with the increase of S_h. This is reasonable because the hydrate has a very low

conductivity similar to the oil (Waite et al., 2009; Frane et al., 2011; Haukalid et al., 2017).

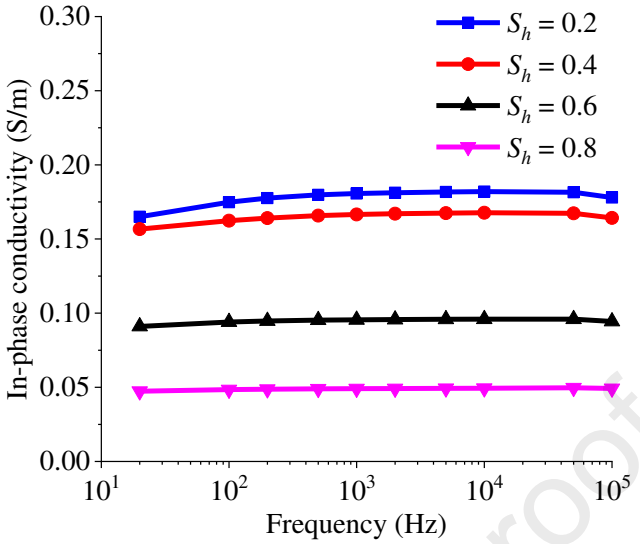

Fig. 6 Variations of the in-phase conductivity for different hydrate saturations with frequency

The formation factor is calculated to be the ratio of the pore-water conductivity to the in-phase conductivity of a fully saturated sample according to the Archie's formula (Eq. (4)). The coefficient a is considered as unity for pure sands as used in the experiments of this work. **Fig. 7** shows the variation of the cementation exponent (m) with the test frequency, as well as the fitting curve and line based on the experimental data. It can be observed that different correlations between m and f can be obtained in the two frequency ranges separated by the critical frequency f_c. Considering the different polarization mechanisms in the lower and higher frequency ranges separated by f_c, it is more sensible to deal with the relations between m and f in different means. The relation between m and f is fitted based on the least-square method in the frequency range $f < f_c$, and an average is obtained in the frequency range $f > f_c$ as shown in Eq. (11). The coefficient of determination (R^2) and root mean square error (E_{RMS}) are provided in the illustrations to show the fitting performance and uncertainty. It needs to be mentioned that the R^2 for the range of $f > f_c$ is not provided because no best-fitting operation was involved. Error bars have been plotted with data points based on the E_{RMS}, However, due to the small amplitude of the E_{RMS}, some of

the error bars have been covered by the markers themselves (as can be seen in the range of $f < f_c$).

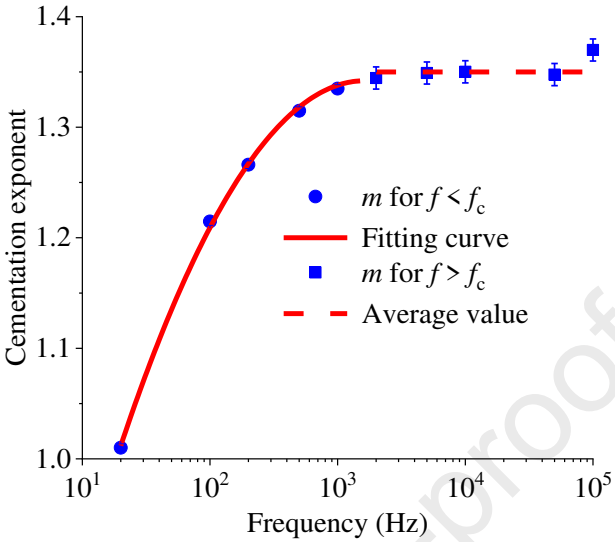

$f < f_c$: $R^2 = 0.999$, E_{RMS} =0.0035; $f > f_c$: $E_{RMS} = 0.010$

Fig. 7 Variations of the cementation exponent (*m*) with frequency (*f*) lower and higher than the critical frequency (f_c = 2 kHz)

$$m = \begin{cases} -0.09(\lg f)^2 + 0.58\lg f + 0.41 & f < f_c \\ 1.35 & f > f_c \end{cases} \tag{11}$$

The conductivity index *I* is calculated as the ratio of the in-phase conductivity of the sample to that of the water-saturated sample following the Archie's formula (Eq. (5)). We can obtain Eqs. (12) and (13) through multiplying Eq. (4) by Eq. (5). **Fig. 8** shows the variations of the lithological coefficient (*b*), saturation exponent (*n*) with the test frequency, as well as the fitting curves and lines based on the experimental data.

$$FI = \frac{\sigma_w}{\sigma_t'} = b\phi^{-m} S_w^{-n} \tag{12}$$

$$\lg\left(\frac{\sigma_w}{\sigma_t'}\right) = -n\lg(S_w) - m\lg(0.4) + \lg(b) \tag{13}$$

where σ_t' is the in-phase conductivity of the hydrate-bearing sandy sample.

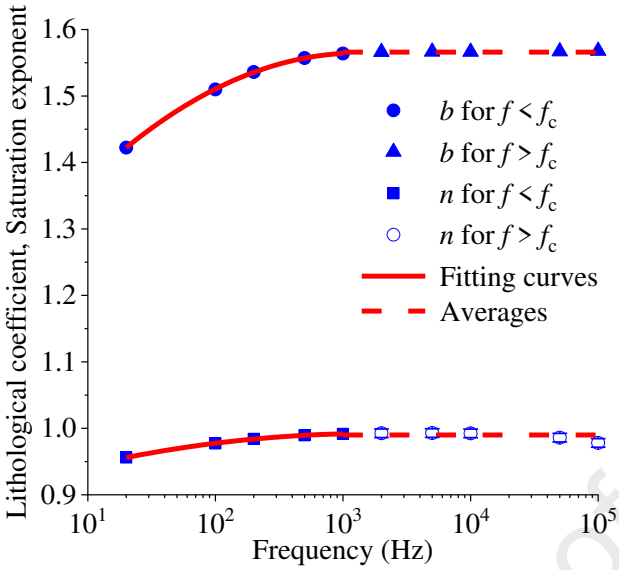

b: $f < f_c$, $R^2 = 0.999$, E_{RMS} =0.0006; $f > f_c$, E_{RMS} = 0.0006

n: $f < f_c$, $R^2 = 0.999$, E_{RMS} =0.0002; $f > f_c$, E_{RMS} = 0.006

Fig. 8 Variations of the lithological coefficient (*b*)and saturation exponent (*n*) with frequency (*f*) lower and higher than the critical frequency (f_c = 2 kHz)

$$b = \begin{cases} -0.04(\lg f)^2 + 0.27\lg f + 1.15 & f < f_c \\ 1.57 & f > f_c \end{cases} \tag{14}$$

$$n = \begin{cases} -0.01(\lg f)^2 + 0.06\lg f + 0.89 & f < f_c \\ 0.99 & f > f_c \end{cases} \tag{15}$$

The frequency higher than f_c is preferred because stable values for m, b and n are expected for a specific sandy sample. Thus, the hydrate saturation for the sandy samples can be calculated from the in-phase conductivity and porosity by using Eq. (16), which is valid in a wide frequency range ($f > f_c$), i.e., from 2 kHz to 100 kHz in this work.

$$\frac{\sigma_w}{\sigma_t'} = 1.57\phi^{-1.35}\left(1 - S_h\right)^{-0.99} \tag{16}$$

An uncertainty analysis of the parameters (m, n and b) in the in-phase conductivity models (i.e., Eqs. (11)-(16)) is carried out below to enhance the confidence in the models for real applications. The first task in the process of

uncertainty analysis is to identify sources of uncertainty, and then determine how they can be characterized in the analysis. Some typical sources of epistemic uncertainty in hydrate-saturation modeling include: measurement errors in the complex conductivity, heterogeneity of the tested hydrate-bearing sample, errors in the reference hydrate saturation, and errors in the besting-fitting operation.

(1) Measurement errors in the complex conductivity. The complex conductivity is computed from the measured impedance and geometrical factor. The uncertainty of the impedance results from the error of the LCR meter and effects of the connecting cables between the electrodes and the LCR meter (i.e., the calibration plane specifically). The uncertainty of the geometrical factor comes from the measurement error of the length and diameter of the samples. It needs to be noted that only the uncertainty of the LCR meter is labeled as 1%, but the rest uncertainty cannot be evaluated quantified accurately. However, it is believed that those uncertainties are of a similar magnitude with that of the LCR meter (Calibration tests on objects of known conductivities or impedances such as NaCl solution and resistor-capacitor network have been performed before the formal hydrate experiments.). The uncertainties may account for the scatter in the measurement results of complex conductivity.

(2) Heterogeneity of the tested hydrate-bearing sample. The heterogeneity of the samples comes from two aspects, i.e., heterogeneity of the skeleton and that of the hydrate. The heterogeneity of the skeleton can be ignored as the size range of the sand particles used in the experiment is narrow (180 – 250 μm). The heterogeneity of hydrate in the porous media has been reported in several experimental and numerical research works, such as Bald et al. (2003), Zhao et al. (2011), Yin et al. (2018ab, 2019ab) and Liu et al. (2019) among others. The complex-conductivity responses of THF-hydrate-bearing sandy samples would be different from that of an ideal sample with no heterogeneity. Therefore, some uncertainties would be introduced into the resultant complex conductivity.

(3) Errors in the reference hydrate saturation. The hydrate saturation is defined as the volume ratio of the hydrate

to pore space of the porous medium. With an assumption that all the added THF has been converted into THF hydrate, the reference hydrate saturation can be calculated by Eq. (8). However, it has been reported that the initial THF cannot be converted into THF hydrate completely in the formation process due to the requirement for achieving a chemical equilibrium in the THF-hydrate-water system (Strauch et al., 2018). Furthermore, the conversion rate is affected by some factors such as the cooling mode or temperature history and initial THF/water ratio (Strauch et al., 2018; Yin et al., 2019a; Liu et al., 2019). Besides the incompleteness of the conversion from the THF to hydrate, parameters in Eq. (8) such as the volume of the sand pack, porosity and masses of the pore water and THF can result in uncertainties of the reference hydrate saturation as well.

(4) Errors in the besting-fitting operation. The parameters (*m*, *n* and *b*) in the in-phase conductivity models were derived from a best-fitting operation based on the experimental data. As a result, there are two sources of uncertainties for the fitting parameters. One of them is the uncertainty resulting from the three sources analyzed above, which propagates into the uncertainties of the model parameters. The other is the essential uncertainty accompanying with the best-fitting algorithm. In this work, we used the coefficient of determination (R^2) and root mean square error (E_{RMS}) to describe the uncertainties of the fitting parameters in the models. Error bars have been plotted with data points involved in the best-fitting operation in the figures (**Figs. 7-10**) based on the E_{RMS}. However, some of the error bars have been covered by the markers due to the small amplitude of the E_{RMS}.

It needs to be mentioned that the above uncertainty analysis also applies to the model presented in **Section 4.3**, because the uncertainties of the two types of models (i.e., the in-phase conductivity model and phase angle model presented in **Section 4.2 and 4.3**, respectively) have the same nature (The uncertainty stems from a best-fitting operation based on the experimental data). Moreover, the first three sources of uncertainties identified above have only been analyzed qualitatively, and the fourth source of uncertainty has been quantified. The effects of the first

three sources have not been left out because the resultant uncertainties have already propagated into the uncertainty due to the fourth source.

4.3 Saturation model based on electrical polarization mechanism

It has been shown in **Section 4.1** that the parameter FE of the phase angle has a definite dependence on the hydrate saturation. It is beneficial to develop the potential to evaluate S_h based on the parameter FE. **Fig. 9a** shows the variations of the phase angle with frequency for different hydrate saturations, i.e., from 0.2 to 0.8. It can be observed that the phase angle for each fixed S_h decreases first and then increases with the increase of the frequency, and the minimum value can be identified around the critical frequency. However, it needs to be noted that the change rate of the phase angle with the frequency are remarkably different for different S_h, especially in the frequency range $f > f_c$. The change rate can be characterized quantitatively by the parameter FE after a designation of the higher and lower frequencies, i.e., f_H and f_L, respectively.

If the frequency 100 Hz is denoted as the fixed f_L, for example, the parameter FE of the phase angle is calculated and plotted against FR in **Fig. 9b** for the frequencies $f > f_c$. The different FR is an indication of the different f_H for a fixed f_L. It needs to be mentioned that the purpose of using the FR instead of f_H is to demonstrate the frequency difference between f_H and f_L more clearly. It can be observed in **Fig. 9b** that the characteristic parameter FE of the phase angle follows a linear relationship with FR. Furthermore, the slope (denoted as k_p hereafter) of the best-fitting line between FE and FR increases monotonously with the increase of S_h. Considering both the parameter FE and k_p exhibit definite dependence on S_h, we correlate FE at a certain FR (corresponding to a certain f_H for a fixed f_L) with S_h and k_p with S_h, respectively. **Fig. 10** demonstrates the linear relationships between FE and S_h as well as between k_p and S_h. It needs to be noted that the logarithms of FE and

k_p are utilized instead of the parameters themselves in order to reduce the adverse effects of the intrinsic nonlinearity between the parameters. Finally, two linear correlations (as shown by Eqs. (17) and (18) serving as hydrate-saturation evaluation models) are derived based on the frequency-dispersion characteristics of the phase angle of complex conductivity.

$$\log_{10}(\mathrm{FE}) = \begin{cases} A_1 S_h - B_1 & \mathrm{FR} = 500 \\ A_2 S_h - B_2 & \mathrm{FR} = 1000 \end{cases} \tag{17}$$

$$\log_{10}(k_p) = C S_h - D \tag{18}$$

where A_1 = 2.687, B_1 = 1.074, A_2 = 1.952, B_2 = 0.257, C = 1.631 and D = 3.005.

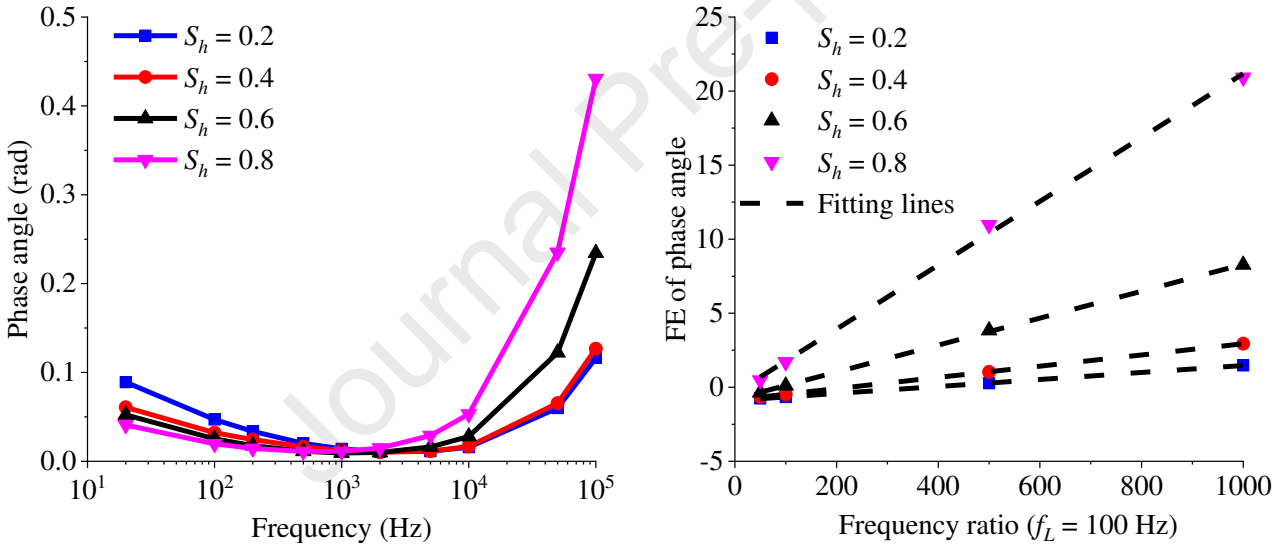

(a) Frequency dispersion of phase angle (b) FE of phase angle against FR at f_L = 100 Hz

S_h = 0.2: R^2 = 0.999, E_{RMS} =0.011; S_h = 0.4: R^2 = 0.999, E_{RMS} =0.015;
S_h = 0.6: R^2 = 0.999, E_{RMS} =0.046; S_h = 0.8: R^2 = 0.998, E_{RMS} =0.472

Fig. 9 Frequency dispersion of the phase angle and relationship between FE and FR for different hydrate saturations

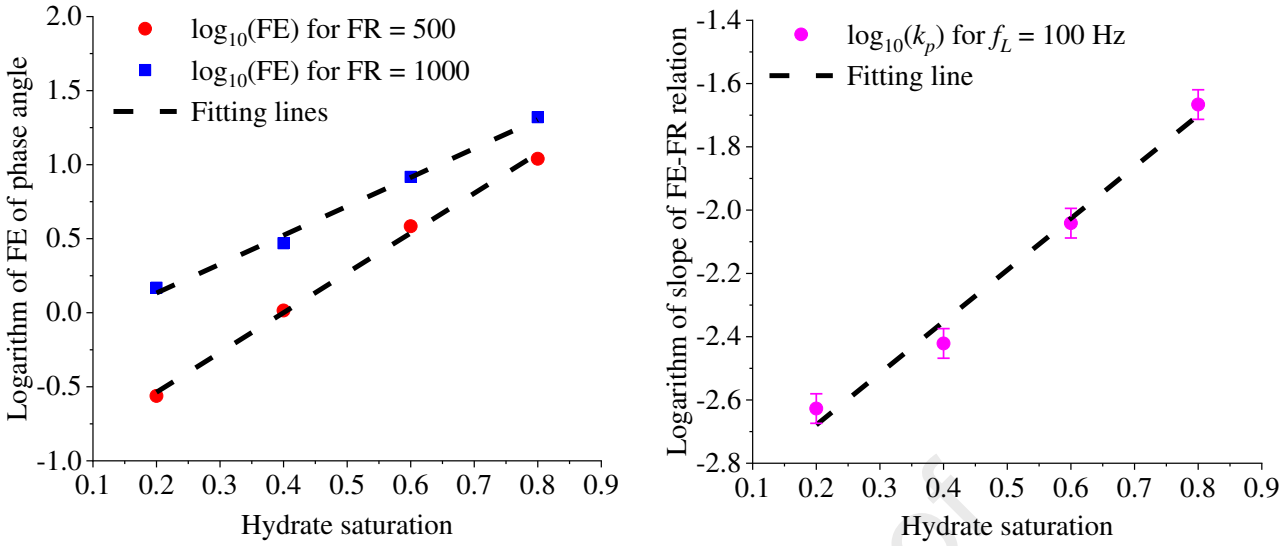

(a) FE of phase angle against hydrate saturation (b) slope of FE-FR relation against hydrate saturation

$\log_{10}$(FE) for FR = 500: R^2 = 0.994, E_{RMS} =0.047;

$\log_{10}$(FE) for FR = 1000: R^2 = 0.997, E_{RMS} =0.046;

$\log_{10}(k_p)$: R^2 = 0.984, E_{RMS} =0.047

Fig. 10 Relationships between FE of the phase angle and hydrate saturation and between the slope of FE-FR relation and hydrate saturation

4.4 Saturation model based on information fusion principle

Two types of hydrate-saturation evaluation models based on different parameters of the complex conductivity have been developed in **Section 4.2 and 4.3**, respectively. The first type of the models is developed based on the in-phase conductivity using the Archie's formula, and the second makes use of the frequency-dispersion characteristic parameters of the phase angle, i.e., FE and k_p. The in-phase conductivity reflects the electrical conductance mechanism, and the phase angle and its frequency-dispersion characteristics correspond to the electrical polarization mechanism. Therefore, the above two types of models are called the conductance-based model and polarization-based model, respectively, in this work.

It is of significance to integrate the two types of models based on the information fusion principle in order to derive a comprehensive model, which takes into account both the electrical conductance and polarization mechanisms. A fusion model based on the complex-conductivity parameters is developed in this section. The flowchart of the model-operation process is presented in **Fig. 11** and introduced below. Firstly, the in-phase conductivity, FE of the phase angle and k_p are computed from the measured complex conductivity of hydrate-bearing samples. Secondly, the conductance-based model (as expressed by Eq. (16)) and polarization-based models (as expressed by Eqs. (17) and (18)) established in **Section 4.2 and 4.3** are used to calculate hydrate saturations, respectively. The outputs of the above two types of models are denoted as S_{hc} and S_{hp}. Thirdly, the arithmetic mean is taken for S_{hc} (at different frequencies) and S_{hp} (for the FE and k_p models), and then denoted as $\overline{S}_{hc}$ and $\overline{S}_{hp}$, respectively. Fourthly, the fusion model with $\overline{S}_{hc}$ and $\overline{S}_{hp}$ as inputs is built based on a specific weighted-average algorithm. The output of the fusion model (denoted as $\hat{S}_h$) is calculated by Eq. (19), which is regarded as the final solution to the hydrate saturation.

$$\hat{S}_h = W\overline{S}_{hc} + (1-W)\overline{S}_{hp} \tag{19}$$

where W is a weighting factor.

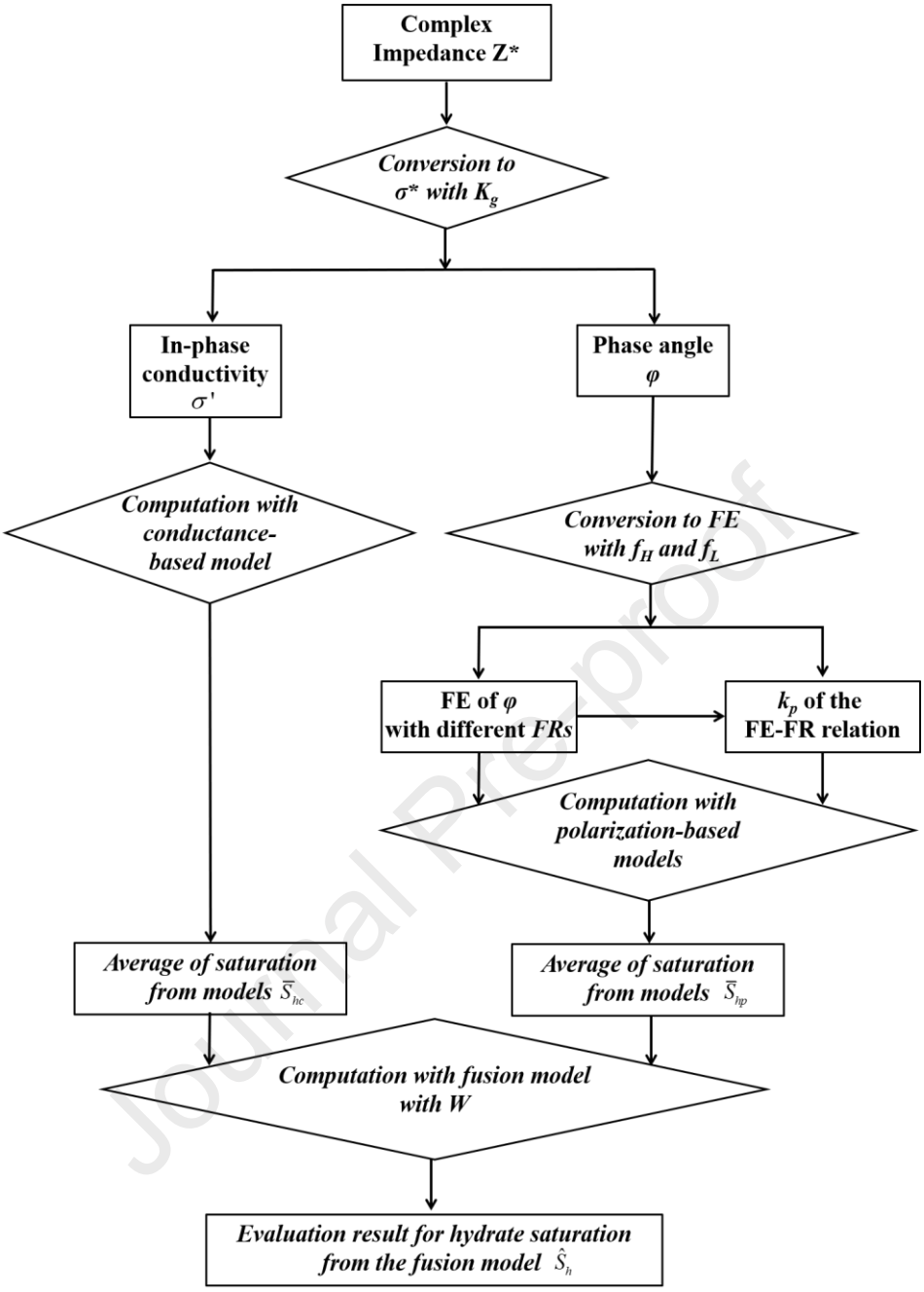

Fig. 11 Flowchart for operating the fusion model based on complex conductivity

4.5 Assessment of hydrate-saturation models

The hydrate saturation has been calculated by the three types of models, i.e., the conductance-based model, polarization-based model and fusion model, and then compared with the reference from the experimental data. The absolute error (E_A) and relative error (E_R) of model predictions for each saturation (i.e., S_h = 0.2, 0.4, 0.6

and 0.8) are calculated with Eqs. (20) and (21). Those error specifications are used to quantify the model performance at a specific test point, i.e., a specific hydrate saturation of the sample. The root mean square error (E_{RMS}) is also computed for each of the models with Eq. (23). The E_{RMS} is used to assess the model performance for the whole test range of hydrate saturations quantitatively, showing the average deviation from the reference saturations for all the tested samples. The model predictions for hydration saturations are compared with experimental measurements in **Fig. 12**. The absolute and relative errors of model predictions are listed in **Table 1** to **Table 8** and the root mean square error is presented in the text below. Error bars are plotted with data points based on the E_{RMS} in **Fig. 12**.

$$E_A = S_{hm} - S_{h0} \tag{21}$$

$$E_R = \frac{S_{hm} - S_{h0}}{S_{h0}} \times 100\% \tag{22}$$

$$E_{RMS} = \sqrt{\frac{1}{N}\sum_{i=1}^{N}\left(S_{hm}(i) - S_{h0}(i)\right)^2} \tag{23}$$

where S_{hm} and S_{h0} are hydrate saturations calculated by the models and obtained from the experimental data (the reference values of hydrate saturations), respectively; N is the counts of the tested samples for each model and i represents the i_{th} sample.

Conductance-based models. The type of conductance-based models includes five separated models, each of which employs the in-phase conductivity at a certain frequency as the input. The frequency ranging from 2 kHz to 100 kHz ($f > f_c$) are taken into account for the five models (f = 2, 5, 10, 50, 100 kHz). It can be seen from **Fig. 12a** and **Table 1** that the relative error E_R decreases sharply with the increase of S_h from 0.2 to 0.8. It changes from 28.8% at S_h = 0.2 to -0.1% at S_h = 0.8. A relatively higher E_R at a lower reference S_h may largely result from the smaller denominator in Eq. (22), thus it is necessary to examine the absolute error E_A simultaneously.

It can be found in **Table 2** that the E_A varies from -0.084 to less than 0.005 at S_h = 0.4 and 0.8, respectively. Generally, a higher E_A appears at the lower saturations such as S_h = 0.2 and 0.4. Both the E_R and E_A show a consistent deviation trend that the errors exhibit the same polarity for each S_h. For example, the E_R and E_A at S_h = 0.2 for all the five models are positive, showing that the model predicted saturations are higher than the reference. The root mean square errors (E_{RMS}) for the five models are all around 0.051. Through a comparison between E_A and E_{RMS} it can be seen that the quite large E_A at lower saturations, i.e., S_h = 0.2 and 0.4, dominates the whole model performance in terms of the E_{RMS}, and the errors at higher saturations can be ignored safely. Three reasons have been identified to account for the characteristics of errors presented above. Firstly, the reference values have higher uncertainty at low saturations, especially for saturations lower than 0.5. A lower conversion rate of the THF to hydrate (Strauch et al., 2018) in the tested samples results in errors of the reference saturation. Secondly, the enhanced heterogeneity for lower hydrate saturations may distort the complex conductivity responses to some extent. Thirdly, some uncertainty may arise from the oversimplification of the Archie's formula, e.g., application of the constant Archie's parameters as indicated in Eqs. (11), (14) and (15).

Polarization-based models. The type of polarization-based models includes three models with the parameters k_p and FE as inputs as shown in Eqs. (17) and (18), respectively. They are denoted as the k_p model, FE model with FR = 500 and FE model with FR = 1000, respectively. It can be observed in **Fig 12b** and **Table 3 and 4** that the absolute and relative errors for the polarization-based models exhibit different behaviors from those for the conductance-based models. Firstly, the E_A and E_R for the polarization-based models is lower than that for the conductance-based models at the same S_h except S_h = 0.8. Secondly, the E_A and E_R have different polarities at the same S_h except S_h = 0.8, which provides an opportunity to reduce the errors by averaging the results. The E_{RSM} for the three models is 0.029, 0.012 and 0.017, respectively, much lower than that for the conductance-

based models. Based on a comparison of the E_{RSM}, we can claim that the models with FE as inputs perform better than the k_p model, and the two FE models are quite consistent with each other. Furthermore, the FE model with FR = 1000 presents a constantly lower E_R than the k_p model for all the tested samples of different S_h. As presented in **Section 4.3** the characteristic parameter k_p is defined as the slope of the FE-FR relation. More uncertainties may be introduced into the k_p model in the derivation process from the FE to k_p. Therefore, it is understandable that the FE models become superior than the k_p model to some extent.

Fusion models. The various fusion models are obtained by adjusting the weighting factor W in Eq. (19) from 0.1 to 0.5. Theoretically, a higher W should be allocated to a more accurate input to obtain a result with more reliability and higher accuracy. The polarization-based models perform better than the conductance-based models in the perspective of a lower E_{RSM}. Therefore, a weighting factor no more than 0.5 is assigned to the input of the fusion models, i.e., the output derived from the conductance-based models. The average values of the outputs from the conductance-based and polarization-based models are denoted as $\overline{S}_{hc}$ and $\overline{S}_{hp}$ respectively. They are used as the raw inputs of the fusion model before the multiplication by their respective weighting factor. It can be seen in **Fig. 12c** and **Table 5 and 6** that, at the same hydrate saturations, the errors increase with an increasing W for S_h = 0.2, 0.4 and 0.6. Conversely, the errors exhibit a decreasing trend with the increase of W for S_h = 0.8. This can be understandable because the polarization-based models perform better than the conductance-based models for S_h = 0.8 as indicated by the lower E_A and E_R. The E_{RSM} for the five fusion models is 0.017, 0.021, 0.024, 0.028 and 0.032, respectively. Considering the lower E_R at $S_h < 0.8$ and the lowest E_{RMS} we select W = 0.1 as the best weighting factor for the selected fusion model (i.e., the fusion model with W = 0.1) in the analysis below.

A comparison among the performance of the three types of models, i.e., the conductance-based model, polarization-based model and fusion model with $W = 0.1$, has been made and shown in **Fig. 12d**. The average of the outputs, i.e., $\overline{S}_{hc}$ and $\overline{S}_{hp}$, from the conductance-based models and polarization models are used for this comparison. It can be observed from **Table 7 and 8** that both the E_A and E_R for the fusion model with $W =$ 0.1 are located between the bounds defined by those for the conductance-based and polarization-based models. The E_{RMS} for the conductance-based, polarization-based and fusion models is 0.051, 0.013 and 0.017, respectively. It is obvious that the incorporation of the conductance-based models into the fusion model results in increased E_A, E_R and E_{RMS} than those for the polarization models. However, there are at least two advantages to use the fusion model rather than the polarization model. Firstly, the selected fusion model is supposed to be more reliable than each of the conductance-based and polarization-based models, because more underlying physics and parameters have been taken into account. Secondly, the degradation of the model performance in the perspective of the error specification (e.g., E_A, E_R and E_{RMS}) can be alleviated by adjusting the weighting factor, which adds more flexibility to the hydrate-evaluation model.

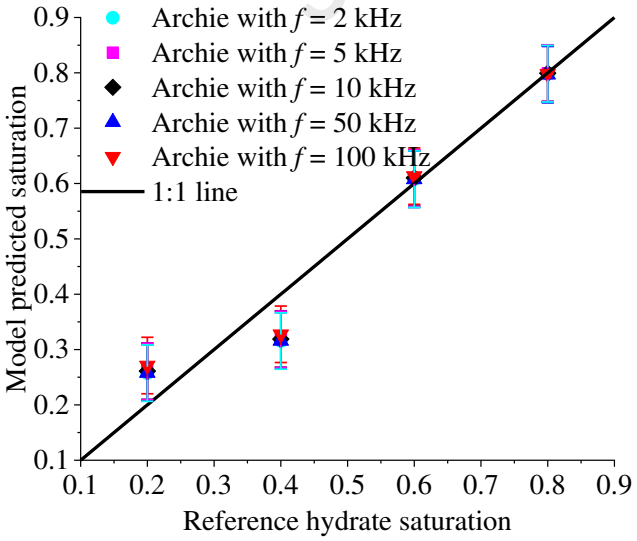

(a) Conductance-based models

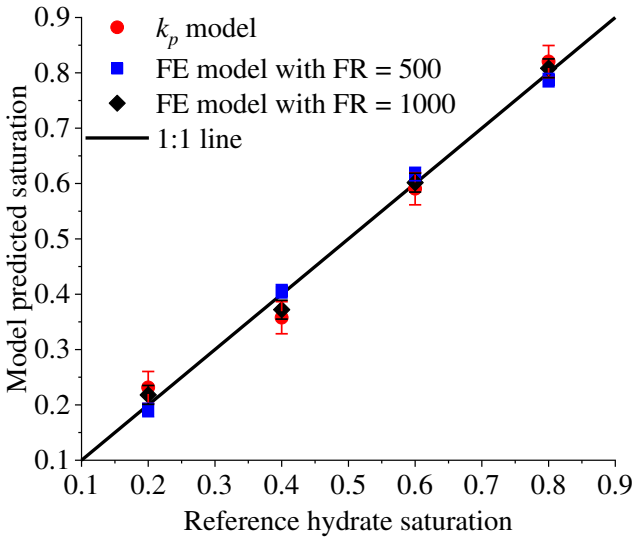

(b) Polarization-based models

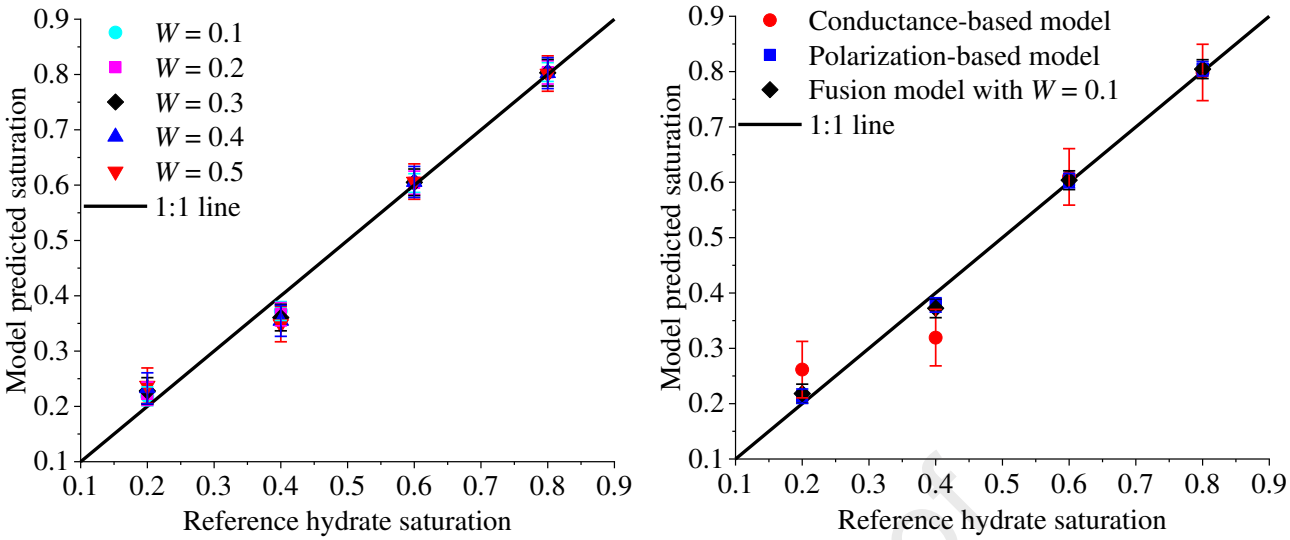

(c) Fusion models (d) Comparison of the three models

Fig. 12 Comparison between the model calculated results and reference hydrate saturations

Table 1 Absolute error (dimensionless) of hydrate saturation predictions from the conductance-based models

	$S_h = 0.2$	$S_h = 0.4$	$S_h = 0.6$	$S_h = 0.8$
f = 2 kHz	0.057	-0.084	0.008	-0.002
f = 5 kHz	0.061	-0.082	0.010	-0.001
f = 10 kHz	0.061	-0.081	0.010	-0.001
f = 50 kHz	0.058	-0.084	0.008	-0.003
f = 100 kHz	0.071	-0.072	0.013	-0.002

Table 2 Relative error (in percent) of hydrate saturation predictions from the conductance-based models

	S_h = 0.2	S_h = 0.4	S_h = 0.6	S_h = 0.8
f = 2 kHz	28.7	-21.1	1.3	-0.2
f = 5 kHz	30.3	-20.4	1.7	-0.1
f = 10 kHz	30.5	-20.3	1.7	-0.1
f = 50 kHz	28.9	-21.1	1.3	-0.4
f = 100 kHz	35.5	-18.1	2.2	-0.2

Table 3 Absolute error (dimensionless) of hydrate saturation predictions from the polarization-based models

	S_h = 0.2	S_h = 0.4	S_h = 0.6	S_h = 0.8
k_p model	0.031	-0.042	-0.009	0.021
FE model with FR = 500	-0.009	0.005	0.017	0.013
FE model with FR = 1000	0.018	0.028	0.002	0.008

Table 4 Relative error (in percent) of hydrate saturation predictions from the polarization-based models

	S_h = 0.2	S_h = 0.4	S_h = 0.6	S_h = 0.8
k_p model	15.7	-10.6	-1.6	2.6
FE model with FR = 500	-4.6	1.3	2.8	1.6
FE model with FR = 1000	9.0	7.0	0.3	1.0

Table 5 Absolute error (dimensionless) of hydrate saturation predictions from the fusion models

	$S_h = 0.2$	$S_h = 0.4$	$S_h = 0.6$	$S_h = 0.8$
$W = 0.1$	0.018	-0.028	0.004	0.005
$W = 0.2$	0.023	-0.034	0.004	0.004
$W = 0.3$	0.028	-0.040	0.005	0.003
$W = 0.4$	0.033	-0.045	0.006	0.002
$W = 0.5$	0.037	-0.051	0.007	0.001

Table 6 Relative error (in percent) of hydrate saturation predictions from the fusion models

	$S_h = 0.2$	$S_h = 0.4$	$S_h = 0.6$	$S_h = 0.8$
$W = 0.1$	9.1	-6.9	0.6	0.6
$W = 0.2$	11.5	-8.4	0.7	0.5
$W = 0.3$	13.9	-9.9	0.9	0.4
$W = 0.4$	16.3	-11.3	1.0	0.3
$W = 0.5$	18.7	-12.8	1.1	0.2

Table 7 Absolute error (dimensionless) of hydrate saturation predictions from the average of the conductance-based models, polarization-based models and selected fusion model

	$S_h = 0.2$	$S_h = 0.4$	$S_h = 0.6$	$S_h = 0.8$
Conductance-based model	0.062	-0.081	0.010	-0.002
Polarization-based model	0.013	-0.022	0.003	0.005
Fusion model with $W = 0.1$	0.018	-0.028	0.004	0.005

Table 8 Relative error (in percent) of hydrate saturation predictions from the average of the conductance-based models, polarization-based models and selected fusion model

	$S_h = 0.2$	$S_h = 0.4$	$S_h = 0.6$	$S_h = 0.8$
Conductance-based model	30.8	-20.2	1.6	-0.2
Polarization-based model	6.7	-5.4	0.5	0.6
Fusion model with $W = 0.1$	9.1	-6.9	0.6	0.6

5 Discussion

5.1 Potential for evaluating hydrate saturation with quadrature conductivity

It has been demonstrated that both the electrical conductance and polarization mechanisms are incorporated in the fusion models for evaluating the hydrate saturation. The models utilize the parameters of complex conductivity, such as the in-phase conductivity, FE and k_p of the phase angle, as the inputs. However, it needs to be mentioned that there are other complex-conductivity parameters, such as the magnitude and quadrature conductivity, that have not been used in the modeling and analysis presented above. The two pairs of parameters of complex conductivity (i.e., the magnitude and phase angle, in-phase and quadrature conductivities) can be converted to each other. However, that does not necessarily mean that the related parameters are as usable as their counterparts in the perspective of hydrate-saturation evaluation capability. Furthermore, a wide frequency ranging from 20 Hz to 100 kHz has been tested in the experiment as introduced in **Section 3**, but only the complex conductivity at frequencies higher than the critical frequency ($f > f_c$) has been used in the actual modelling and hydrate-saturation calculation presented above. Actually, there are more possibilities to develop more hydrate-saturation models to make a full use of the plentiful information of complex-conductivity responses. As a result, the fusion model will be capable of incorporating more information, parameters and underlying physics and be expected to achieve a more reliable prediction of the hydrate saturation in the complicated natural sediments (as demonstrated in **Section 4.5**).

The quadrature conductivity is a counterpart parameter of the phase angle, because both of them are responsible for the electrical polarization mechanism. Similar characteristics and relationship with the hydrate saturation to those of the phase angle have been identified. This shows a great potential for evaluating the hydrate saturation with the quadrature conductivity. However, some issues come up hindering the modeling procedure.

Fig. 13a shows the variations of the quadrature conductivity with frequency at different S_h, i.e., from 0.2 to 0.8 (see **Fig. 9** for reference). It can be observed that the quadrature conductivity at frequencies lower than the critical frequency ($f < f_c$) shows its capability to discriminate the different S_h. However, the quadrature conductivity in the higher frequency range is not sensitive to the variations of S_h at all. The parameter FE of the quadrature conductivity is then plotted versus FR with f_L = 20 Hz for different S_h in Fig. **13b**. It can be seen in **Fig. 13b** that the parameter FE follows a nonlinear trend with the increase of FR, which is different from the linear relation for the phase angle as indicated in **Fig. 9b**. Furthermore, it needs to be noted that the FE of quadrature conductivity varies non-monotonically with S_h at a fixed FR. Consequently, it is rather difficult to correlate either the FE or the slop of FE-FR relation with S_h, as done for the phase angle. Further experimental and theoretical investigations should be carried out to address those issues for developing new types of models to evaluate the hydrate saturation based on the quadrature conductivity.

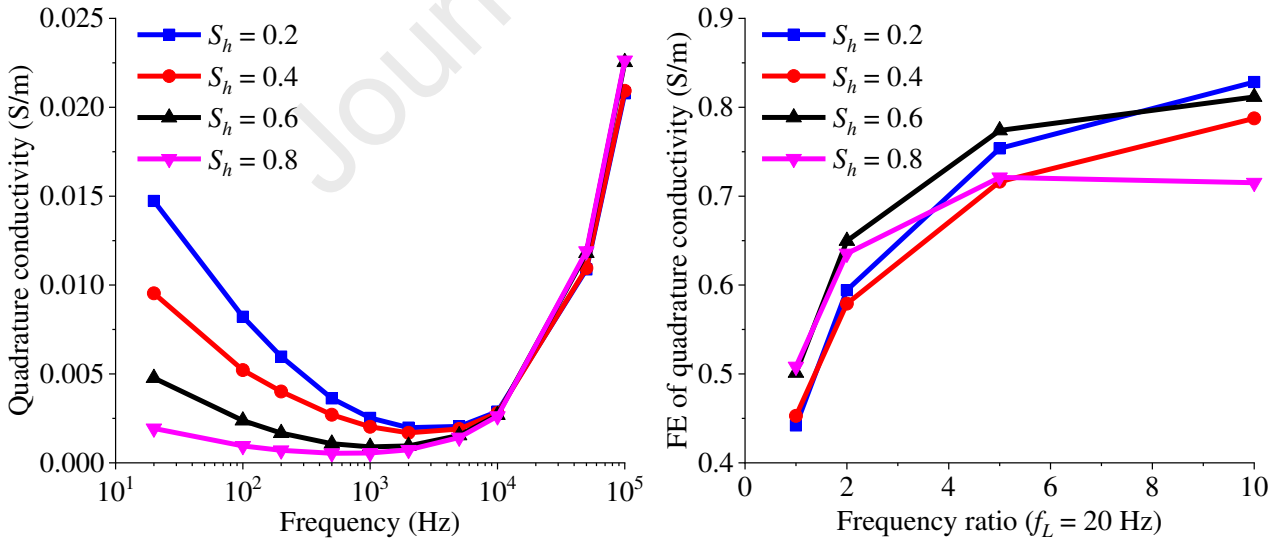

(a) Frequency dispersion of quadrature conductivity (b) FE of quadrature conductivity against FR

Fig. 13 Frequency dispersion of quadrature conductivity and relation between FE and FR for different hydrate saturations

5.2 Effectiveness and advances of using THF as hydrate former

The THF has been widely used as a hydrate former in laboratory studies for preparing samples to simulate gas hydrate-bearing sediments. Various physical properties (e.g., electromagnetic, thermal and mechanical) have been investigated to gain more insights to the gas hydrate or gas hydrate-bearing sediments (Pearson et al., 1986; Santamarina and Ruppel, 2008; Cortes et al., 2009; Yun et al., 2007; Lee et al., 2007; 2010ab; Liu et al., 2019; Wu et al., 2021a). There are indeed differences between the THF hydrate and gas hydrates (e.g., methane hydrate predominantly formed in natural sediments), such as the crystal structures (i.e., Structure II for THF and Structure I structure for methane, (Sloan, 1998)) and polarizability of the guest molecules (i.e., polar molecule for THF and nonpolar molecule for methane). However, it has been shown that, for laboratory artificial samples, the hydrate formation scheme (involving, e.g., chemical and thermodynamic properties of the pore water, physical-chemical properties and stress state of the mineral particles, history of pressure and temperature variations, relative amounts and mixing sequence/state of all the phases) and produced pore-scale spatial distribution of hydrates play a more important role in affecting the macroscale properties (e.g., mechanical, electrical etc.) of hydrate-bearing samples than the differences between THF and methane hydrates themselves (Lee et al., 2007; Priest et al., 2009; Zhang et al., 2001).

The effectiveness of using the THF hydrate as an analogue to methane hydrate in the experiments in terms of kinetic formation processes, physical properties and pore-scale spatial distributions (locations relative to the mineral particles) are summarized as below. First, THF is completely immiscible with water, thereby the kinetic formation process of THF hydrate resembles that in the deep sediments within the gas hydrate stability zones, where the hydrate formed with dissolved gas (e.g., aqueous phase methane) in pore water (Buffett and Zatsepina,

2000; Spangenberg et al., 2005; Lee et al., 2007). Second, the dielectric permittivity of THF is as low as that of nonpolar molecules due to the large size of THF molecules (Lee et al., 2007). There is no significant difference in the electrical properties (i.e., electrical conductivity and dielectric permittivity) of THF and methane hydrates. Third, the interfacial tension between water and either THF or methane hydrate is similar, thereby it is expected that THF and methane hydrates have similar growth patterns in water-saturated sediments (i.e., resembling typical gas hydrate-bearing environments). It has been indicated by acoustic wave velocities that the hydrates formed from dissolved methane or THF solution behave as a frame-building component at a hydrate saturation above 40% and exhibit a pore-filling behavior below 40% (Spangenberg et al., 2005; Priest et al., 2009).

There are many advantages to use the THF as a hydrate former in the laboratory investigations. First, as the THF is completely immiscible with water, the time required by the hydrate-formation process in laboratory studies can be shortened significantly compared with that for gas hydrate. Due to the low solubility of methane gas into water, the kinetic formation process of methane hydrate is restricted by the slow transport of methane via diffusional or advective processes (Lee et al., 2007). Second, the THF hydrate can form at conditions of a moderate temperature (e.g., below 4.4 □) and standard atmospheric pressure (i.e., 101325 Pa) (Makinoet al., 2005; Conrad et al., 2009). Consequently, the experimental costs and risks can be suppressed significantly. Therefore, more experimental conditions and tests can be realized conveniently. Third, the hydrate saturation (or volume fraction) in sediments can be controlled closely to some extent, and a relatively homogeneous hydrate-bearing samples can be obtained. This claim is a bit controversial and the related issues will be discussed in **Section 5.3**.

Bearing the effectiveness and advantages of using the THF as a hydrate former discussed above in mind, we

designed and carried out our experiments on the THF hydrate-bearing sandy samples (**Section 3**). However, it is of profound importance to identify and discuss some issues with regard to the characterization of THF hydrate-bearing samples and the modelling for hydrate-saturation evaluation (**Section 5.3**).

5.3 Issues related to THF hydrate-bearing samples

There are two major issues related to the THF hydrate-bearing samples tested for complex-conductivity responses in this work, i.e., assumptions of a complete conversion rate of THF and homogeneous distribution of THF hydrate in porous media. The first assumption is that all the THF added into the pore water of the sand sample can be transformed into THF hydrate in the experiment, based on which the reference hydrate saturation is obtained. The second assumption is that the THF hydrate is distributed homogeneously in the sandy samples, based on which the effects of the heterogeneity of samples on the complex conductivity are not taken into account.

The first question is whether all the THF has been converted into THF hydrate. If there was still some THF in the remaining water in the pores, the reference hydrate saturation calculated from the initial ratio of the THF to water directly would be inaccurate. Furthermore, the remaining THF in the pore water at the end of the hydrate formation process would affect the complex-conductivity responses to some extent. Some uncertainties would be subsequently introduced into the fitting parameters of the hydrate-evaluation models (**Section 4**) in this work. It has been reported by Strauch et al. (2018) that there are differences between theoretically expected (i.e., calculated from the initial ratio of the THF to water as did in this work) and effectively obtained volume fractions of the THF hydrate due to the requirement for a chemical equilibrium in the system. Both THF-excess and H_2O-excess cases were investigated in their work and it was claimed that the deviations of the resultant THF-hydrate

saturation increased with a decreasing aspired saturation for the two cases. Then they proposed corrections to calculate the actual hydrate amount after the formation process based on their results. The analysis and correlations presented by Strauch et al. (2018) seem to provide an answer to our question, however, it has to be noted that the system they worked on only include THF, water and THF hydrate. In our work there are sand particles in the test system besides the THF, water and THF hydrate. Furthermore, the differences in the hydrate formation procedure such as the cooling mode or temperature history would affect the cage occupancy as well as the final conversion rate of the THF to hydrate (Strauch et al., 2018; Yin et al., 2019a; Liu et al., 2019). Conversely, a complete transformation from the THF solution to hydrate was reported with the aid of magnetic resonance imaging (MRI) visualization (Baldwin et al., 2003). To summarize, it is still an open question to accurately quantify the conversion rate of the THF to hydrate and thus the actual hydrate saturation for the initial THF-water-sediment system. Multiple measurement techniques such as X-ray CT and MRI, estimations from thermal signatures and numerical simulations based on hydrate-formation kinetic models are recommended to characterize the hydrate formation process and quantify the actual hydrate saturation.

The second question is whether the THF hydrate has been distributed in the porous medium homogeneously. If the heterogeneity of the skeleton of the sand pack is ignored (It is reasonable due to the narrow range of the size of sand particles used in the experiment.), but the THF hydrate is distributed inhomogeneously in the pores of the sandy sample, the complex-conductivity responses of the THF hydrate-bearing sand sample would deviate from those of an ideal sample with no heterogeneity. It is inevitable that some uncertainties would be introduced into the parameters of the hydrate-evaluation models (**Section 4**) in this work. The heterogeneity of THF hydrate formed in clays has been noted in the work of Liu et al. (2019), where the hydrate distribution and morphology were visualized with X-ray CT. It has been shown that the THF hydrate formed in clays is segregated and

heterogeneous, no longer as a pore constituent as in sandy sediments. Moreover, the uniformly distributed hydrate tends to be obtained with the samples experiencing larger subcooling temperatures. In this work we used fine sands with a diameter range of 180-250 μm to simulate the sediments, where the THF hydrate would form as a pore constituent that results in much less heterogeneity than that in clays (Liu et al., 2019). Experimental studies were conducted on THF hydrates in bulk solution, sandstone or quartz glass beads by Bald et al. (2003) and Zhao et al. (2011), where direct visualizations on samples in the formation and dissociation processes were performed by using MRI. It was shown that MRI was an effective tool for determining the spatial distribution of the hydrate and non-hydrate phases in the samples. There are differences in the processes of nucleation, growth, and dissociation between gas hydrates and the THF hydrate; however, the formed crystals of THF hydrate resemble the heterogeneous and fracture morphology of gas hydrates in clays (Liu et al., 2019). The heterogeneity in spatial distributions of the phase saturations for methane hydrate-bearing samples made in laboratory was demonstrated numerically in a series of works by Yin et al. (2018ab, 2019ab). It has been shown that the spatial distributions of various phases at the end of the methane-hydrate formation process are strongly heterogeneous (Yin et al., 2018b). Additionally, the assumption of initial homogeneity in the phase saturation results in large deviations in the temperature and cumulative amounts of the produced gas and water at the early stage and consistently unreliable pressure compared with experiments in the whole stage of the production process (Yin et al., 2019b). The numerical simulation plays an irreplaceable role in characterizing the sample heterogeneity in the absence of direct measurement techniques such as X-CT (Jin et al., 2007; Seol and Kneafsey, 2011; Liu et al., 2019; Wu et al., 2020; Liang et al., 2021) or MRI (Bald et al., 2003; Zhao et al., 2011), and in optimizing the design of experimental apparatus and formation scheme for creating hydrate-bearing samples (Yin et al., 2019a). Wu et al. (2020) proposed a pore-scale 3D (three dimensional) morphological algorithm for constructing hydrate-bearing-sediment models, and then examined the effects of the hydrate saturation and

occurrence habits on the physical properties of hydrate-bearing samples including the electrical conductivity. To examine the effects of the micro-distribution mode of hydrates in the pores on the electrical properties of porous media, we have developed 2D numerical models based on the finite element method (Xing et al., 2021). It has been demonstrated that the in-phase conductivity exhibits significant variations under the same saturation and salinity but different micro-distribution modes. The variations can be attributed to the change in the tortuosity of electrical conduction paths in the void space of porous media. Further work needs to be carried out on the influence of the micro/macro-scale heterogeneity on the quadrature conductivity of the samples.

5.4 Extension to samples with gas, higher salinity and under stress

Another issue to be discussed is that there is no gas in THF hydrate-bearing samples in this work (Wu et al., 2021a). There are four phases, i.e., the solid skeleton, hydrate, aqueous solution (water) and gas, coexisting in a gas hydrate-bearing sample. Based on the underlying principle of complex conductivity, we can expect more complicated complex-conductivity responses due to the more phases and more complex interfaces among them in the sample. Firstly, if only the electrical conductance mechanism is considered, the measured in-phase conductivity is to be influenced by the concentration and distribution of both the hydrate and gas simultaneously. This is because both the hydrate and gas can be regarded as insulators, which can affect the paths of the electrical conductance significantly. Secondly, if only the electrical polarization mechanism is considered, the measured quadrature conductivity is also to be affected by the hydrate and gas. The interfacial polarization, which is responsible for the quadrature conductivity in the frequency range $f > f_c$ (**Section 4.1**), is caused by the formation of free-charge distributions near the interfaces between different components due to the discontinuity of dielectric permittivity. The dielectric constant of gas can be designated as 1, but that of the hydrate varies with the test frequency (Lee et al., 2007; Waite et al. 2009; Haukalid et al., 2017). However, it is a common practice

that the interfaces between the hydrate and gas as well as between the water and hydrate/gas are considered to be uncharged (Leroy et al., 2008; Jougnot et al., 2010). Consequently, the main influencing factor still stems from the properties of the interface between the pore water and skeleton. To sum up, due to the similar electrical properties of hydrate and gas, it is still a challenge for both the in-phase and quadrature conductivities to distinguish between them directly. An integrated analysis of the electrical and acoustic properties of gas hydrate-bearing samples is recommended to deal with the four-phase system (Lee and Collet, 2008; Xing et al., 2020).

The salinity of the pore water in hydrate-bearing formations in the fields varies around 3.0 % to 3.5 % by mass for typical oceanic locations (Collett and Ladd, 2000; Riedel et al., 2006; Lee and Collet, 2008, 2009; Wang et al., 2011a, 2011b). In this work, we used NaCl solution with a mass fraction of 1.0 % in the experiments (at the end of the hydrate formation process). There are two reasons to use the lower-salinity pore water in this work. The first reason is to alleviate the challenge to form the hydrate in sands because the salt is an inhibitor to hydrate formation. The temperature at the phase-equilibrium boundary decreases with the increase of the pore-water salinity. Consequently, a lower temperature has to be maintained for the preparation of hydrate-bearing sandy samples at higher pore-water salinities. The second one is that the effects of the pore-water conductivity on the quadrature conductivity of porous media can be neglected if the pore-water conductivity exceeds 1.0 S/m (Revil and Skold, 2011; Niu et al., 2016). The salinity of the 1.0 % NaCl solution corresponds to a conductivity of 0.97 S/m (at 4.5 □). In addition, it has been demonstrated that the in-phase conductivity of hydrate-bearing sands can be modelled by the Archie's formula properly with the pore-water salinity of 1.0 % in this work. Considering the decreasing influence of the surface conductivity with the increase in the pore-water conductivity (Klein and Santamarina, 2003), it is more reasonable to apply the Archie's model to cases with higher salinities (e.g., 3.5 %). To summarize, due to the negligible effects of the higher salinity on the quadrature conductivity

and the capability of the Archie's formula for modelling the in-phase conductivity, the experimental results and models for the hydrate-saturation evaluation obtained at a specific salinity of 1.0 % still possess general significance for higher salinities.

The stress state of hydrate-bearing sediments is one of the influencing factors to the physical properties, especially to the mechanical properties of the samples. The effective confining stress, i.e., the difference between the confining pressure and the pore pressure, represents the surrounding effective stress governed by the overlying and surrounding sediments (Wu et al., 2021a). In this work, we have been focusing on the complex electrical properties of the hydrate-bearing sands. The in-phase component of complex conductivity reflects contributions of the solid particles, bulk pore fluid and additional surface conduction due to the EDL, while the quadrature conductivity results from the contribution of the polarization of the EDL coating the surface of solid particles. The contribution of the pore fluid is affected by several factors, such as the porosity, tortuosity and hydrate pore habit. The porosity and tortuosity are influenced by the (effective) confining pressure because an elevation of the (effective) confining pressure results in a drop of the porosity as well as variation of the shape of pore space. In addition, the hydrate pore habit is affected by the effective stress applied to the skeleton of sediments (Dai et al., 2012). Furthermore, both the conduction along particle surfaces (i.e., surface conductivity) and the quadrature conductivity are influenced by the surface state, which can be altered by the pore habit of hydrates. For instance, in comparison with the fluid-suspending mode where the hydrate has no contact with the particles, the attachment of hydrate clusters on the particles in the grain-attaching mode (Xing et al., 2021) may result in an increase in the tortuosity of the surface conduction path and a decrease of the surface area coated by the EDL. As a result, the in-phase and quadrature conductivity may be elevated and reduced, respectively, in the grain-attaching mode of hydrates.

6 Conclusions

It is proposed to characterize the electrical properties of hydrate-bearing porous media and evaluate the hydrate saturation based on parameters of complex conductivity. The tetrahydrofuran (THF) hydrate is synthesized in sands, forming samples for the measurement of the complex-conductivity responses at different hydrate saturations. Frequency-dispersion characteristics of the complex conductivity for the hydrate-bearing samples are analyzed and hydrate-saturation evaluation models are established based on parameters of the complex conductivity.

(1) The complex conductivity of hydrate-bearing samples is measured in the frequency range of 20 Hz – 100 kHz. A critical frequency (f_c = 2 kHz) can be identified, where extreme values are obtained for the phase angle and imaginary component of the complex conductivity. It is postulated that the electrical-double-layer polarization and interfacial polarization (Maxwell-Wagner effect) are the dominant polarization mechanisms for the frequency lower and higher than the critical frequency, respectively.

(2) The hydrate-saturation evaluation models are derived based on the in-phase conductivity and frequency-dispersion characteristic parameters of the phase angle at frequencies higher than the critical frequency. The Archie's formula can be used to model the relationship between the in-phase conductivity and hydrate saturation. Two linear correlations between the logarithms of FE or k_p and hydrate saturation can be established serving as hydrate-saturation evaluation models.

(3) The conductance-based (with the in-phase conductivity as the input) and polarization-based models (with the phase angle as the input) are integrated based on the information fusion principle. The best performance in

the perspective of low errors and high reliability for evaluating the hydrate saturation can be obtained with the fusion model. This can be contributed to the information fusion principle, which incorporates more parameters of the complex conductivity and underlying physics of the electrical conductance and polarization into this model.

(4) The quadrature conductivity in the frequency range lower than the critical frequency also shows remarkable frequency-dispersion characteristics. However, the parameter FE varies non-monotonically with the hydrate saturation, posing difficulties for deriving a hydrate-saturation evaluation model. It deserves more investigations to develop the potential for evaluating the hydrate saturation based on parameters of the complex conductivity in the frequency range lower than the critical frequency.

A new approach for evaluating the hydrate saturation in porous media has been demonstrated experimentally in this work. However, based on the discussion in **Section 5**, there is still much challenging and interesting work to conduct for enhancing its capability of evaluating gas hydrate-bearing sediments. To develop the potential of the quadrature conductivity for predicting the hydrate saturation, further experimental and theoretical investigations should be carried out. The numerical modelling is a great means to characterize the hydrate-bearing samples to account for the influences of the non-completeness of the THF conversion to hydrate and micro/macro-scale heterogeneity on the complex electrical conductivity. Furthermore, to push the proposed approach into real applications it is necessary to take into account the effects of the gas phase in the pore space, effective stress on the skeleton, size distribution of the particles as well as clays in the hydrate-bearing porous media.

Acknowledgement

The authors would like to express sincere thanks to the financial support by the Fundamental Research Funds for the Central Universities (20CX05005A and 18CX02112A), the Major Scientific and Technological Projects of CNPC (ZD2019-184-001), PetroChina Innovation Foundation (2018D-5007-0214), Shandong Provincial Natural Science Foundation (ZR2019MEE095, ZR2017BEE026) and National Natural Science Foundation of China (51306212, 41704124). We are sincerely grateful to the editor and five anonymous referees for their constructive comments.

The data relating to this work are available and can be shared by contacting the corresponding author.

References

Archie, G.E., 1942. The electrical resistivity log as an aid in determining some reservoir characteristics, *Transactions of the AIME,* 146(01), 54–62.

Baldwin, B. A., Moradi-Araghi, A., Stevens, J. C., 2003. Monitoring hydrate formation and dissociation in sandstone and bulk with magnetic resonance imaging. *Magnetic Resonance Imaging*, 21(9), 1061–1069.

Breede, K., Kemna, A., Esser, O., Zimmermann, E., Vereecken, H., Huisman, J. A., 2012. Spectral induced polarization measurements on variably saturated sand-clay mixtures, *Near Surface Geophysics*, 10(6), 479–489.

Chelidze, T. L., Gueguen, Y., 1999. Electrical spectroscopy of porous rocks: a review—I. Theoretical models. *Geophysical Journal International*, 137(1): 1–15.

Chelidze, T. L., Gueguen, Y., Ruffet, C., 1999. Electrical spectroscopy of porous rocks: a review—II. Experimental results and interpretation. *Geophysical Journal International*, 137(1): 16–34.

Chen, Y., Or, D., 2006. Geometrical factors and interfacial processes affecting complex dielectric permittivity of partially saturated porous media, *Water Resources Research*, 42, W06423, 1–9.

Chen, Y., Or, D., 2006. Effects of Maxwell-Wagner polarization on soil complex dielectric permittivity under variable temperature and electrical conductivity, *Water Resources Research*, 42, W06424, 1–14.

Cole, K.S., Cole, R.H., 1941. Dispersion and absorption in dielectrics I. Alternating current characteristics, *The Journal of Chemical Physics*, 9(4), 341–351.

Collett, T.S., 2002. Energy resource potential of natural gas hydrates, *AAPG Bulletin*, 86(11), 1971–1992.

Collett, T.S., Ladd, J., 2000. Detection of gas hydrate with downhole logs and assessment of gas hydrate concentrations (saturations) and gas volumes on the Blake Ridge with electrical resistivity log data. Proceedings of the Ocean Drilling Program, Scientific Results, 164, 179–191.

Conrad, H., Lehmkuhler, F., Sternemann, C., Sakko, A., Paschek, D., Simonelli, L., Huotari, S., Feroughi, O., Tolan, M., Hamalainen, K., 2009. Tetrahydrofuran clathrate hydrate formation. *Physical Review Letters*, 103(21), 218301.

Cook A.E., Anderson B.I., Rasmus J., Sun, K., Li, Q., Collet, T., Goldberg, D., 2012. Electrical anisotropy of gas hydrate-bearing sand reservoirs in the Gulf of Mexico, *Marine and Petroleum Geology*, 34(1), 72–84.

Cook, A. E., Waite, W. F., 2018. Archie's saturation exponent for natural gas hydrate in coarse-grained reservoirs, *Journal of Geophysical Research: Solid Earth*, 123, 2069–2089.

Cortes, D. D., Martin, A. I., Yun, T. S., Francisca, F. M., Santamarina, J. C., Ruppel, C., 2009. Thermal conductivity of hydrate□bearing sediments. *Journal of Geophysical Research*, 114, B11103.

Dai, S., Santamarina, J. C., Waite, W. F., Kneafsey, T. J., 2012. Hydrate morphology: Physical properties of sands with patchy hydrate saturation. *Journal of Geophysical Research: Solid Earth*, 117, B11205.

Denicol, P. S., Jing, X.D., 1998. Effects of water salinity, saturation and clay content on the complex resistivity of sandstone samples, *Geological Society of London Special Publications*, 136(1), 147–157.

Denicol, P. S., Jing, X.D., 1996. Estimation of permeability of reservoir rocks from complex resistivity data, *Trans. 37th SPWLA Symp.* New Orleans, LA, June 16–19.

Du Frane, W. L., Stern, L. A., Weitemeyer, K. A., Constable, S., Pinkston, J. C., Roberts, J. J., 2011. Electrical properties of polycrystalline methane hydrate, *Geophysical Research Letters*, 38(9),1-5.

Freedman, R., Vogiatzis, J. P., 1986. Theory of induced-polarization logging in a borehole, *Geophysics*, 51(9), 1830–1849.

Haukalid, K., Folgerø, K., Barth, T., Fjermestad, S. L., 2017. Hydrate formation in water-in-crude oil emulsions studied by broad-band permittivity measurements, *Energy & Fuels*, 31(4), 3793-3803.

Jiang, M., Ke, S., Kang, Z., 2018. Measurements of complex resistivity spectrum for formation evaluation, *Measurement*, 124,359–366.

Jin, Y., Hayashi, J., Nagao, J., Suzuki, K., Minagawa, H., Ebinuma, T., Narita, H., 2007. New method of assessing absolute permeability of natural methane hydrate sediments by microfocus X□ray computed

tomography. *Japanese Journal of Applied Physics*, 46(5A), 3159–3162.

Jougnot, D., Ghorbani, A., Revil, A., Leroy, P., Cosenza, P., 2010. Spectral induced polarization of partially saturated clay-rocks: a mechanistic approach, *Geophysical Journal International*, 180(1), 210–224.

Kennedy, W.D., Herrick, D.C., 2003. Conductivity anisotropy in shale-free sandstone, *Petrophysics*, 45(1), 38–58.

Klein, K. A., Santamarina, J. C., 2003. Electrical conductivity in soils: underlying phenomena. *Journal of Environmental and Engineering Geophysics*, 8(4), 263–273.

Koh C. A., Sum, A. K. E., Sloan, E. D., 2012. State of the art: Natural gas hydrates as a natural resource, *Journal of Natural Gas Science and Engineering*, 8, 132–138.

Liu, Z., Kim, J., Lei, L., Ning, F., Dai, S., 2019. Tetrahydrofuran hydrate in clayey sediments–laboratory formation, morphology, and wave characterization. *Journal of Geophysical Research Solid Earth,* 124(4), 3307–3319.

Lee, J Y, Yun, T S, Santamarina, J C, Ruppel, C., 2007. Observations related to tetrahydrofuran and methane hydrates for laboratory studies of hydrate□bearing sediments. *Geochemistry, Geophysics, Geosystems*, 8(6), Q06003.

Lee, J. Y., Santamarina, J. C., Ruppel, C., 2010a. Parametric study of the physical properties of hydrate-bearing sand, silt, and clay sediments: 1. electromagnetic properties, *Journal of Geophysical Research: Solid Earth*, 115, B11104.

Lee J. Y., Francisca F. M., Santamarina J. C., Ruppel C., 2010b. Parametric study of the physical properties of hydrate-bearing sand, silt, and clay sediments: 2. small-strain mechanical properties. *Journal of Geophysical Research*, 115, B11105.

Lee, M.W., Collett T.S., 2008. Integrated analysis of well logs and seismic data to estimate gas hydrate concentrations at Keathley Canyon, Gulf of Mexico, *Marine and Petroleum Geology*, 25(9), 924–931.

Lee, M.W., Collett, T.S., 2009. Gas hydrate saturations estimated from fractured reservoir at Site NGHP-01-10, Krishna-Godavari Basin, India, *Journal of Geophysical Research: Solid Earth*, 114(B7), 261–281.

Lee, M.W., Hutchinson, D.R., Collett, T. S., and Dillon, W. P., 1996. Seismic velocities for hydrate-bearing sediments using weighted equation, *Journal of Geophysical Research: Solid Earth*, 101(B9), 20347–20358.

Leroy, P., Revil, A., Kemna, A., Cosenza, P., Ghorbani, A., 2008. Complex conductivity of water-saturated packs of glass beads, *Journal of Colloid and Interface Science*, 321(1), 103-117.

Li, J., Ke, S., Yin, C., Kang, Z., Jia, J., Ma, X., 2019. A laboratory study of complex resistivity spectra for predictions of reservoir properties in clear sands and shaly sands, *Journal of Petroleum Science and Engineering*,

177, 983–994.

Liang, H., Yang, L., Song, Y., Zhao, J., 2021. New approach for determining the reaction rate constant of hydrate formation via X-ray computed tomography. *The Journal of Physical Chemistry C*, 125(1): 42–48.

Liu, C., Meng, Q., Hu, G., Li, C., Sun, J., He, X., Wu, N., Yang, S., Liang, J., 2017. Characterization of hydrate-bearing sediments recovered from the Shenhu area of the South China Sea. *Interpretation*, 5(3), 13–23.

Liu, C., Ye, Y., Meng, Q., He, X., Lu, H., Zhang, J., Liu, J., Yang, S., 2012. The characteristics of gas hydrates recovered from Shenhu area in the South China Sea. *Marine Geology*, 307-310, 22–27.

Liu, Z., Kim, J., Lei, L., Ning, F., Dai, S., 2019. Tetrahydrofuran hydrate in clayey sediments—Laboratory formation, morphology, and wave characterization, *Journal of Geophysical Research: Solid Earth*, 124, 3307–3319.

Lysne, P.C, 1983. A model for the high-frequency electrical response of wet rocks, *Geophysics*, 48(6), 775–786.

Makino, T., Sugahara, T., Ohgaki, K., 2005. Stability boundaries of tetrahydrofuran + water system. *Journal of Chemical & Engineering Data*, 50(6), 2058–2060.

Makogon, Y.F., 2010. Natural gas hydrates – a promising source of energy, *Journal of Natural Gas Science and Engineering*, 2(1), 49–59.

Milkov, A.V., 2004. Global estimates of hydrate-bound gas in marine sediments: how much is really out there?, *Earth-Science Reviews*, 66(3-4), 183–197.

Moridis, G. J., Collett, T. S., Boswell, R., Kurihara, M., Reagan, M. T., Koh, C. A., Sloan E. D., 2009. Toward production from gas hydrates: current status, assessment of resources, and simulation-based evaluation of technology and potential. *SPE Reservoir Evaluation & Engineering*, 12(5), 745–771.

Moridis, G. J., Collett, T. S., Pooladi-Darvish, M., Hancock, S., Santamarina, C., Boswell, R., Kneafsey, T., Rutqvist, J., Kowalsky, M. B., Reagan, M. T., Sloan, E. D., Sum, A. K., Koh, C. A., 2011. Challenges, uncertainties and issues facing gas production from gas hydrate deposits. *SPE Reservoir Evaluation & Engineering*, 14(1), 76–112.

Moss, A., Jing, X., Archer, J., 2002. Wettability of reservoir rock and fluid systems from complex resistivity measurements, *Journal of Petroleum Science and Engineering*, 33(1), 75–85.

Ning, F., Zhang K., Wu N., Zhang, L., Li, G., Jiang, G., Yu, Y., Liu, L., Qin, Y., 2013a. Invasion of drilling mud into gas-hydrate-bearing sediments. Part I: effect of drilling mud properties, *Geophysical Journal International*, 193(3), 1370–1384.

Ning, F., Wu N., Yu, Y., Zhang K., Jiang, G., Zhang, L., Sun, J., Zheng, M., 2013b. Invasion of drilling mud into gas-hydrate-bearing sediments. Part II: effects of geophysical properties of sediments, *Geophysical Journal*

International, 193(3), 1385–1398.

Niu, Q., Revil, A., Saidian, M., 2016. Salinity dependence of the complex surface conductivity of the Portland sandstone. *Geophysics*, 81(2), D125–D140.

Norbisrath, J. H., Weger, R. J., Eberli, G. P., 2017. Complex resistivity spectra and pore geometry for predictions of reservoir properties in carbonate rocks, *Journal of Petroleum Science and Engineering*, 151, 455–467.

Nordsiek, S., Weller, A., 2008. A new approach to fitting induced-polarization spectra, *Geophysics*, 73(6), 235–245.

Osterman, G., Keating, K., Binley, A., Slater, L., 2016. A laboratory study to estimate pore geometric parameters of sandstones using complex conductivity and nuclear magnetic resonance for permeability prediction, *Water Resources Research*, 52(6), 4321–4337.

Pearson, C., Murphy, J., Hermes, R., 1986. Acoustic and resistivity measurements on rock samples containing tetrahydrofuran hydrates: laboratory analogues to natural gas hydrate deposits. *Journal of Geophysical Research Solid Earth*, 91(B14), 14132–14138.

Priest, J. A., Best, A. I., Clayton, C.R.I., 2005. A laboratory investigation into the seismic velocities of methane gas hydrate-bearing sand, *Journal of Geophysical Research: Solid Earth*, 110, B04102

Priest, J. A., Rees, E. V. L., Clayton, C. R. I., 2009. Influence of gas hydrate morphology on the seismic velocities of sands, *Journal of Geophysical Research: Solid Earth*, 114, B11205.

Revil, A., Linde, N., Cerepi, A., Jougnot, D., Matthäi, S., Finsterle, S., 2007. Electrokinetic coupling in unsaturated porous media, *Journal of Colloid and Interface Science*, 313(1), 315–327.

Revil, A., Eppehimer, J. D., Skold, M., Karaoulis, M., Godinez, L., Prasad, M., 2013. Low-frequency complex conductivity of sandy and clayey materials, *Journal of Colloid and Interface Science*, 398, 193–209.

Revil, A., 2013. On charge accumulation in heterogeneous porous rocks under the influence of an external electric field, *Geophysics*, 78(4), 271–291.

Revil, A., Coperey, A., Deng, Y., Cerepi, A., Seleznev, N., 2017a. Complex conductivity of tight sandstones, *Geophysics*, 83(2), 1–80.

Revil, A., Coperey, A., Shao, Z., Florsch, N., Fabricius, I. L., Deng, Y., *et al*., 2017b. Complex conductivity of soils, *Water Resources Research*, 53(8), 7121–7147.

Revil, A., Skold, M., 2011. Salinity dependence of spectral induced polarization in sands and sandstones. *Geophysical Journal International*, 187(2), 813–824.

Riedel, M., Collett, T. S., Hyndman R. D., 2005. Gas hydrate concentration estimates from chlorinity, electrical resistivity and seismic velocity, *Geological Survey of Canada*, *Open File*, 4934, 1–36.

Riedel, M., Long, P. E., Collett T. S., 2006. Estimates of in situ gas hydrate concentration from resistivity monitoring of gas hydrate bearing sediments during temperature equilibration. *Marine Geology*, 227, 215–225.

Ruffet, C., Gueguen, Y., Darot, M., 1991. Complex conductivity measurements and fractal nature of porosity. *Geophysics*, 56(6), 758–768.

Santamarina, J. C., Dai, S., Terzariol, M., Jang, J., Waite, W. F., Winters, W. J., Nagao, J., Yoneda, J., Konno, Y., Fujii, T., Suzuki, K., 2015. Hydro-bio-geomechanical properties of hydrate-bearing sediments from Nankai Trough. *Marine and Petroleum Geology*, 66(2), 434–450.

Santamarina, J. C., Ruppel, C., 2008. The impact of hydrate saturation on the mechanical, electrical, and thermal properties of hydrate□bearing sand, silts, and clay. paper presented at the 6th International Conference on Gas Hydrate, Vancouver, British Columbia, Canada, July 6–10.

Shankar, U., Riedel, M., 2011. Gas hydrate saturation in the Krishna–Godavari basin from P-wave velocity and electrical resistivity logs, *Marine and Petroleum Geology*, 28(10), 1768–1778.

Shepard, F.P., 1954. Nomenclature based on sand-silt-clay ratios. *Journal of Sedimentary Petrology*, 24, 151–158.

Sloan, E. D., Jr., 1998. Clathrate Hydrates of Natural Gases, Marcel Dekker, New York.

Seol, Y., Kneafsey, T. J., 2011. Methane hydrate induced permeability modification for multiphase flow in unsaturated porous media. *Journal of Geophysical Research*, 116, B08102.

Spangenberg, E., 2001. Modeling of the influence of gas hydrate content on the electrical properties of porous sediments, *Journal of Geophysical Research: Solid Earth*, 106(B4), 6535–6548.

Spangenberg, E., Kulenkampff, J., 2006. Influence of methane hydrate content on electrical sediment properties, *Geophysical Research Letters*, 33(24), 1–5.

Spangenberg, E., Kulenkampff, J., Naumann, R., Erzinger, J., 2005. Pore space hydrate formation in a glass bead sample from methane dissolved in water. *Geophysical Research Letters*, 32, L24301.

Strauch, B., Schicks, J., Luzi-Helbing, M., Naumann, R., Herbst, M., 2018. The difference between aspired and acquired hydrate volumes - a laboratory study of THF hydrate formation in dependence on initial THF: H_2O ratios. Journal of Chemical Thermodynamics, 117, 193–204.

Tarasov, A., Titov, K., 2013. On the use of the Cole-Cole equations in spectral induced polarization, *Geophysical Journal International*, 195(1), 352–356.

Tong, M., Tao, H., 2008. Permeability estimating from complex resistivity measurement of shaly sand reservoir, *Geophysical Journal International*, 173(2), 733–739.

Tréhu, A. M., Stakes, D. S., Bartlett, C. D., Chevallier, J., Duncan, R. A., Goffredi, S. K., Potter, S. M., Salamy,

K. A., 2003. Seismic and seafloor evidence for free gas, gas hydrates, and fluid seeps on the transform margin offshore Cape Mendocino. *Journal of Geophysical Research: Solid Earth*, 108(B5), 2263.

Tréhu, A. M., Long, P. E., Torres, M. E., et al., 2004. Three□dimensional distribution of gas hydrate beneath the seafloor: Constraints from ODP Leg 204. *Earth and Planetary Science Letters*, 222(3-4), 845–862.

Tréhu, A. M., Ruppel, C., Holland, M. D., Dickens, G. R., Torres, M. E., Collett, T. S., Goldberg, D., Schultheiss, P., 2006. Gas hydrates in marine sediments: Lessons from scientific ocean drilling, *Oceanography*, 19, 124–142.

Uchida, T., Tsuji, T., 2004. Petrophysical properties of natural gas hydrates□bearing sands and their sedimentology in the Nankai trough. *Resource Geology*, 54(1), 79–87.

Vinegar, H. J., Waxman, M. H., 1984. Induced polarization of shaly sands, *Geophysics*, 49(8), 1267–1287.

Waite, W. F., Santamarina, J. C., Cortes, D. D., Dugan, B., Espinoza, D. N., Germaine, J., et al., 2009. Physical properties of hydrate-bearing sediments, *Reviews of Geophysics*, 47(4), 1-38.

Wang, X., Hutchinson, D. R., Wu, S., Yang, S., Guo, Y., 2011a. Elevated gas hydrate saturation within silt and silty clay sediments in the Shenhu area, South China Sea. *Journal of Geophysical Research: Solid Earth*, 116(B5), B05102.

Wang, X., Wu, S., Lee, M., Guo, Y., Yang, S., Liang, J., 2011b. Gas hydrate saturation from acoustic impedance and resistivity logs in the Shenhu area, South China Sea. Marine and Petroleum Geology, 28(9), 1625–1633.

Waxman, M. H., Smits, L.J.M., 1968. Electrical conductivities in oil-bearing shaly sands, *Society of Petroleum Engineers Journal*, 8(2), 107–122.

Weller, A., Nordsiek, S., Debschütz, W., 2010. Estimating permeability of sandstone samples by nuclear magnetic resonance and spectral-induced polarization, *Geophysics*, 75(6), 215–226.

Winters, W. J., Waite, W. F., Mason, D. H., Gilbert, L. Y., Pecher, I. A., 2007. Methane gas hydrate effect on sediment acoustic and strength properties, *Journal of Petroleum Science and Engineering*, 56(1-3), 127–135.

Worthington, P. F., Collar, F. A., 1984. Relevance of induced polarization to quantitative formation evaluation, *Marine and Petroleum Geology*, 1(1), 14–26.

Wu, P., Li, Y., Sun, X., Liu, W., Song, Y., 2020. Pore□scale 3D morphological modeling and physical characterization of hydrate□bearing sediment based on computed tomography. *Journal of Geophysical Research: Solid Earth*, 125(12), e2020JB020570.

Wu, P., Li, Y., Sun, X., Liu, W., Song, Y., 2021a. Mechanical characteristics of hydrate-bearing sediment: a review. *Energy & Fuels*, 35(2), 1041–1057.

Wu, P., Li, Y., Wang, L., Wang, L., Sun, X., Liu, W., Song, Y., 2021b. Triaxial tests on the overconsolidated

methane hydrate-bearing clayey-silty sediments. *Journal of Petroleum Science and Engineering*, 206, 109035.

Xing, L., Zhu, T., Niu, J., Liu, C., Wang, B., 2020. Development and validation of an acoustic-electrical joint testing system for hydrate-bearing porous media, *Advances in Mechanical Engineering*, 12(3), 1–11.

Xing, L., Qi, S., Xu, Y., Wang, B., Lao, L., Wei, W., Han, W., Wei, Z., Ge, X., Aliyu, A. M., 2021. Numerical study on complex conductivity characteristics of hydrate-bearing porous media. *Journal of Natural Gas Science and Engineering*, 104145.

Yang, M., Zhao, J., Zheng, J., Song, Y., 2019. Hydrate reformation characteristics in natural gas hydrate dissociation process: A review. *Applied Energy*, 256, 113878.

Yin, Z.Y., Moridis, G. J., Chong, Z. R., Linga, P., 2018a. Numerical analysis of experimental studies of methane hydrate dissociation induced by depressurization in a sandy porous medium, *Applied Energy*, 230, 444–459.

Yin, Z.Y., Moridis, G. J., Chong, Z. R., Linga, P., 2019a. Effectiveness of multi-stage cooling processes in improving the CH_4-hydrate saturation uniformity in sandy laboratory samples, *Applied Energy*, 250, 729–747.

Yin, Z.Y., Moridis, G. J., Linga P., 2019b. On the importance of phase saturation heterogeneity in the analysis of laboratory studies of hydrate dissociation, *Applied Energy*, 255, 113861.

Yin, Z.Y., Moridis, G. J., Tan, H. K., Linga, P., 2018b. Numerical analysis of experimental studies of methane hydrate formation in a sandy porous medium. *Applied Energy*, 220, 681–704.

Yun, T. S., Santamarina, J. C., Ruppel, C., 2007. Mechanical properties of sand, silt, and clay containing tetrahydrofuran hydrate. *Journal of Geophysical Research*, 112, B04106.

Zhang, H.Q., Yang, S.X., Wu, N.Y., Su, X., Holland, M., Schultheiss, P., Rose, K., Butler, H., Humphrey, G., GMGS-1 Science Team, 2007. Successful and surprising results for China's first gas hydrate drilling expedition. Fire in the Earth, Methane Hydrate Newsletter, National Technology Laboratory, US department of Energy, Fall Issue, 6–9.

Zhang, W., Creek, J.L., Koh, C.A., 2001. A novel multiple cell photo-sensor instrument: principles and application to the study of THF hydrate formation. *Measurement Science and Technology*, 12, 1620–1630.

Zhang, Y., Park, H., Nishizawa, O., Kiyama, T., Liu, Y., Chae, K., Xue, Z., 2017. Effects of fluid displacement pattern on complex electrical impedance in Berea sandstone over frequency range 10^4–10^6 Hz, *Geophysical Prospecting*, 65(4), 1053–1070.

Zisser, N., Nover, G., 2009. Anisotropy of permeability and complex resistivity of tight sandstones subjected to hydrostatic pressure. *Journal of Applied Geophysics*, 68(3), 356–370.

Highlights

- A critical frequency (f_c = 2 kHz) separating the EDL and Maxwell-Wagner polarization dominant zones in the complex-conductivity spectrum of hydrate-bearing sands is identified.

- Two types of hydrate-saturation evaluation models are derived based on the in-phase conductivity and frequency-dispersion characteristic parameters of the phase angle, respectively.

- The conductance- and polarization-based models are integrated based on the information-fusion principle and a fusion model with a higher accuracy and reliability is obtained.

- The quadrature conductivity in the frequency range lower than the critical frequency shows remarkable frequency-dispersion characteristics with the variation of the hydrate saturation.

Declaration of competing interest

The authors declare that they have no known competing financial interests or personal relationships that could have appeared to influence the work reported in this paper.

The authors:

Lanchang Xing, Jiale Niu, Shuli Zhang, Shengchang Cao, Bin Wang, Liyun Lao, Wei Wei, Weifeng Han, Xinmin Ge, Zhoutuo Wei